http://lib.uliege.be https://matheo.uliege.be

þÿA new auroral structure on Jupiter: Jupiter s auroral b

Auteur : Pardo Cantos, Irene
Promoteur(s) : Grodent, Denis
Faculté : Faculté des Sciences
Diplôme : Master en sciences spatiales, à finalité approfondie
Année académique : 2018-2019
URI/URL : http://hdl.handle.net/2268.2/7581

Avertissement à l'attention des usagers :

Tous les documents placés en accès ouvert sur le site le site MatheO sont protégés par le droit d'auteur. Conformément aux principes énoncés par la "Budapest Open Access Initiative"(BOAI, 2002), l'utilisateur du site peut lire, télécharger, copier, transmettre, imprimer, chercher ou faire un lien vers le texte intégral de ces documents, les disséquer pour les indexer, s'en servir de données pour un logiciel, ou s'en servir à toute autre fin légale (ou prévue par la réglementation relative au droit d'auteur). Toute utilisation du document à des fins commerciales est strictement interdite.

Par ailleurs, l'utilisateur s'engage à respecter les droits moraux de l'auteur, principalement le droit à l'intégrité de l'oeuvre et le droit de paternité et ce dans toute utilisation que l'utilisateur entreprend. Ainsi, à titre d'exemple, lorsqu'il reproduira un document par extrait ou dans son intégralité, l'utilisateur citera de manière complète les sources telles que mentionnées ci-dessus. Toute utilisation non explicitement autorisée ci-avant (telle que par exemple, la modification du document ou son résumé) nécessite l'autorisation préalable et expresse des auteurs ou de leurs ayants droit.

Université de Liège
Faculté des Sciences
Département d'Astrophysique, de Géophysique et d'Océanographie
Laboratoire de Physique Atmosphérique & Planétaire
Research Unit STAR

A new auroral structure on Jupiter
Jupiter's auroral bridge

MASTER'S THESIS

Irene PARDO CANTOS

Supervisor:

Denis GRODENT

Master's Thesis submitted for the degree of Master in Space Sciences
2018/2019

Acknowledgements

This Master's Thesis is the result of a huge personal work. Nevertheless, it would not have been possible without the important support of all the people that have accompanied me in this long and difficult journey.

Los primeros a los que quiero agradecer la posibilidad de estar aquí hoy es a mi familia, principalmente a mis padres, por haber sufrido conmigo y haber hecho que me levante en los momentos más difíciles y por hacer posible mi sueño, porque yo sé que vuestro esfuerzo ha sido igual o superior al mío. A mi hermano, por hacer que los días que nos vemos sean de los mejores de mi vida, por ser un ejemplo a seguir y por estar orgulloso de tu hermana pequeña. He conseguido todo esto gracias a vosotros.

Al resto de mi familia y amigos, que aunque estemos a dos mil kilómetros de distancia, siempre os siento muy cerca. Gracias Jorge por tu gran generosidad.

À Alex, mon compagnon de vie, de rires et de souffrances. Merci d'avoir beaucoup plus de force et de courage que moi et de me les transmettre quand j'en ai besoin. Merci de m'apprendre chaque jour et de vouloir apprendre avec moi. Tu me montres que je suis capable de beaucoup plus.

Thanks Tobias to have had courage to read this whole document and principally to show me that real friends arrive when you least expect it. Thank you, and Alex, to have sung when it was necessary.

À Aurélien, Tess et Juliette, merci de m'avoir accompagnée dans beaucoup de moments très difficiles et de faire partie de ma famille en Belgique.

À Françoise, Stéphan et Laurence, merci de m'avoir accueillie chaque dimanche et de m'avoir acceptée aussi vite. Merci pour la confiance que vous avez placée en moi.

To Amedeo and Mari-Liis, my international family in this two-years adventure. Thanks to have been there and to have shared your confesions with me, to have said nonsenses when it was necessary and to have made this last years so special. I wish you a lot of luck, success, but principally, happiness in this new period of our lives.

Finalement, je ne peux pas oublier les personnes qui ont fait partie de ma vie dans ces derniers mois et qui m'ont acceptée comme une autre collègue. Merci Gilles Wautelet, Jessy Matar, Zhonghua Yao, Guy Munhoven, Louis François, Benoît Hubert, Jean-Claude Gérard, Maïté Dumont, Angela Della Vecchia, spécialement à Bertrand Bonfond et Benjamin Palmaerts pour leurs importants conseils et à Denis Grodent, pour être plus qu'un promoteur. Merci de m'avoir appris et d'avoir placé autant de confiance en moi. Merci de m'avoir encouragée à « mordre sur ma chique ».

Como ya dije una vez y lo repito, tener la oportunidad de estudiar y aprender es el mejor regalo que se le puede hacer a quien quieres, porque el conocimiento nos hace grandes y nos ayuda a apreciar lo que nos rodea. Gracias mamá y papá.

Abstract

The intense auroral emissions of Jupiter are well studied. However, there is still a lot of information to discover. In this study, a structure of the northern hemisphere has been analysed. It has been named Jupiter's auroral bridge since it connects the duskside main emission and the polar region. This structure is not always visible. Three cases with different characteristics were therefore selected in order to analyse the behaviour of this feature. This study is based on the ultraviolet images obtained by the Space Telescope Imaging Spectrograph (STIS) on board the Hubble Space Telescope (HST). The analysis required mapping the locations where this structure appears in the ionosphere towards the equatorial plane in the magnetosphere. To do so, two different methods of mapping were considered. This data could help to infer the origin of this auroral emission. Moreover, in order to estimate its contribution to the total emitted power, the power radiated by the auroral bridge was also analysed. During this study, it was observed that this structure moves equatorward with time and that it pulsates. The periodicity was consequently estimated. This study offers some preliminary results which will be used to characterise Jupiter's auroral bridge; a structure which has been little studied so far.

Contents

Chapter 1

Introduction

The main objective of this study is to identify and characterise an auroral structure of Jupiter using ultraviolet (UV) images collected by the cameras on-board the Hubble Space Telescope. This structure appears poleward of the main auroral emission. In previous studies, this feature has been identified as the arc-like feature of the polar active region [Grodent, 2014] or the noon active region [Nichols et al., 2017]. In this work it will be referred to as Jupiter's **auroral bridge**. Analysing some parameters such as its location, intensity, and periodicity may give insight into the origin of the auroral bridge. An overview of Jupiter, its magnetosphere, and its auroral emissions are provided in this introduction. Thereafter, the methods used for the study, as well as the results obtained and the conclusions that have been extracted are going to be detailed in the following sections.

1.1 Overview of Jupiter

Jupiter could be considered as the centre of a planetary system since it has the same components as a star. Nevertheless, during its formation, the mass did not grow enough to ignite thermonuclear reactions and become a star. Furthermore, Jupiter has the most intense magnetic field, producing the most spectacular auroral emissions in the solar system [Clarke et al., 2004].

Even though it is the biggest and the heaviest planet in the solar system, its rotation period is the shortest, being around 10 hours. Due to its distance from the Sun (5.2 AU, 1 AU = 1 Astronomical Unit $\approx 1.5 \cdot 10^8$ km), the orbital period of Jupiter is about 12 Earth years. Jupiter's rotation is said to be differential because cloud bands rotate at different velocities with latitude. In order to characterise its solid rotation period, the magnetic field is used since it is controlled by the interior of the planet. This planet does not undergo significant changes between seasons because its spin axis is only tilted around 3^{o} with respect to its orbital plane.

Among the 79 confirmed natural satellites orbiting around the Jovian planet (only 53 of them are named) [NASA, d], four of them have awaken scientists' interest, the Galilean moons: Io, Europa, Ganymede, and Callisto, discovered in 1610 by Galileo.

Jupiter is a gas giant, since it is composed of gases; principally hydrogen (86%) and helium (13.6%), which is a similar composition to the Sun. Methane (CH_4), ammonia (NH_3), ammonium hydrosulfide (NH_4SH), and water are also present in traces. Nevertheless, only 2% of the Sun's mass is constituted of heavy elements, while Jupiter has between 3 and 13%. The quantity and distribution of these elements could help to understand the formation of the solar system [Taylor et al., 2004], hence why the Jovian system draws scientists' attention.

Parameter	**Value**
R_{eq} (km)	$71,492 \pm 4$
R_{pol} (km)	$66,854$
M (kg)	$1.8986 \cdot 10^{27}$
ρ (g cm^{-3})	1.326
P_{rot} (h)	9.92496
P_{orb} (years)	11.86
ω (rad s^{-1})	$1.76 \cdot 10^{-4}$
Obliquity (^{o})	3.13
Eccentricity	0.048
Semi-major axis (AU)	5.20

Table 1.1. Physical and orbital parameters of Jupiter [Bagenal and Wilson, 2016; Palmaerts, 2013; Grodent, 2019; NASA, d].

Jupiter was formed from a gas cloud that contracted, converting gravitational energy into its current warm interior ($\approx$ 20000 K). The planet is still contracting around 3 cm per year [Guillot et al., 2004]. In lower layers of the atmosphere, pressure and temperature increase, producing the condensation of the hydrogen and forming an ocean of H. It is thought that half way to Jupiter's core, the pressure rises so much that electrons are separated from the hydrogen nuclei producing liquid metallic hydrogen, which behaves like an electrical conductor [NASA, d]. This electrically conducting fluid in convective motion creates a dynamo. Thanks to the Juno mission, it is suggested that the internal dynamo in Jupiter could occur in the molecular hydrogen layer during the transition to the metallic hydrogen state [Bolton et al., 2017b].

Its clouds make up 71 km of its atmosphere and they are organised in three layers: the top one is likely to be composed of ammonia ice, which provides the famous colours of its atmosphere, the middle layer may be made of ammonium hydrosulfide crystals, and the deepest one is probably made of water vapour and ice [NASA, d].

In 1979, the Voyager 1 Spacecraft discovered that Jupiter's very faint rings are composed of dust, instead of ice as in the case of Saturn's rings. These rings could have been formed by dust coming from the innermost moons of the Jovian system [NASA, d].

Since Jupiter is a gas giant, it does not have a solid surface. This is why spacecraft can not land on it. Moreover, it is not possible to fly into the planet without being harmed due to the huge temperatures and pressure which would melt and destroy any current spacecraft [NASA, d]. Nevertheless, scientists have conveniently defined Jupiter's surface as the altitude where pressure is equal to 1 bar, i.e. where NH_3 clouds are formed and which roughly corresponds with the altitude of Jupiter's sharp visible limb [Grodent, 2019].

1.2 Coordinate systems

Since Jupiter is not a rocky or icy planet where one could define solid geographical coordinates (longitude and latitude), other coordinate systems are used in order to account for the differential rotation of its atmosphere. In this study, the coordinate systems that have been used are the System III and the Local Time.

1.2.1 System III

As the rotation of the Jovian atmosphere is differential, the rotation of the planet is defined as the rotation of its magnetic field, which is fixed to the interior of Jupiter [Bagenal and Wilson, 2016]. Therefore, the spin period is 9.92496 hours (see Table 1.1). This coordinate system is thus fixed to the magnetic field. The X-axis is called the Prime Meridian and it corresponds to the latitude $\theta_{III} = 0^{o}$ and longitude $\lambda_{III} = 0^{o}$; the Z-axis corresponds to the spin axis of the planet; and the Y-axis is the cross product $X \times Z$. Longitudes λ_{III} increase in a clockwise sense [Bagenal and Wilson, 2016].

The longitude of the Prime or Central Meridian is called CML for Central Meridian Longitude and corresponds to the Earth-Jupiter vector [Bagenal and Wilson, 2016] (also known as sub-Earth longitude).

1.2.2 Local Time

This coordinate system is fixed regarding the position of the Sun. Local Time (LT) can be expressed in degrees or in hours [Bagenal and Wilson, 2016]. To work only with positive angles, 360^{o} are added if the angle is negative. Regarding the hours, noon (12 h) corresponds to 0 degrees longitude, dusk (18 h) to 90^{o}, midnight (00 h) LT would be 180^{o} longitude, and dawn (06 h), 270^{o} [Bagenal and Wilson, 2016], as shown in Figure 1.1.

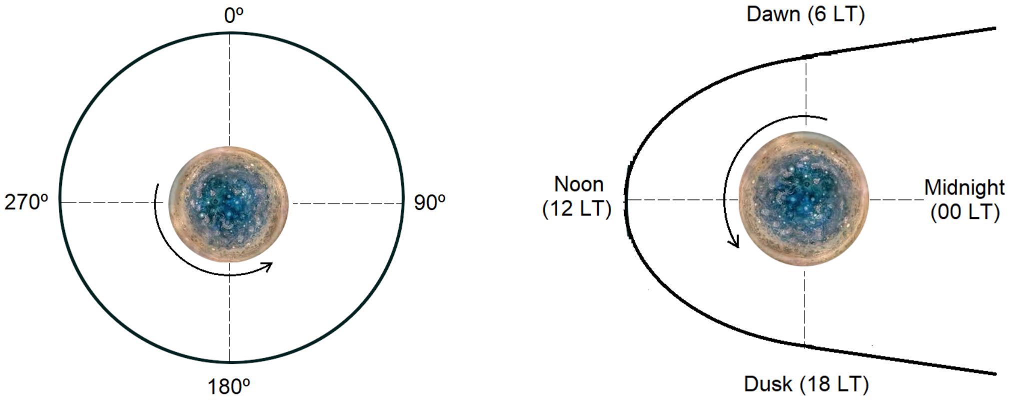

Figure 1.1. Left: Jupiter System III left-handed, X-Y plane. Right: Jupiter Local Time. Equatorial plane. Not to scale.

1.3 Magnetic field and magnetosphere

Jupiter's magnetic field is the most intense in the solar system. The surface magnetic field can reach $\approx$ 4 Gauss in the equatorial region of Jupiter and up to $\approx$ 20 Gauss near the north magnetic pole and $\approx$ 12 Gauss near the south magnetic pole. This strong surface magnetic field and the consequent magnetosphere are created by the dynamo effect and the fast rotation of the planet [Khurana et al., 2004; Connerney et al., 2018]. Jupiter's magnetic field rotates with the planet, catching and accelerating electrically charged particles to high energies. This creates powerful radiation belts, similar to the Earth's Van Allen belts, but millions of times more powerful, which reach some of the Jovian moons and damage spacecraft. Thanks to this intense magnetic field, Jupiter's aurorae are the most incredible in the solar system, emitting auroral powers of 10^{12} W [Grodent, 2014].

In order to understand the dynamo mechanism of a planet, the induction equation has to be employed. This equation describes the temporal evolution of a magnetic field in an electrically conductive fluid, such as plasma.

$$\frac{\partial \mathbf{B}}{\partial t} = D_m \nabla^2 \mathbf{B} + \nabla \times (\mathbf{u} \times \mathbf{B}) \tag{1.1}$$

Where the first term is the magnetic diffusion term and the second one is the magnetic convection term, **B** is the magnetic field and **u** is the speed of the plasma in the frame at rest with the planet. The term $D_m = \frac{1}{\sigma \mu_0}$ is the magnetic diffusivity, where the constants σ and μ_0 are the electric conductivity and the magnetic permeability respectively [Cravens, 1997].

In ideal magnetohydrodynamics (MHD), the conductivity is infinite, so the plasma is said frozen in the field because each ionised particle is attached to a magnetic field line [Cravens, 1997].

On the contrary, if it is the second term that becomes zero, i.e., there is no fluid motion (**u** = 0), then the magnetic field decreases exponentially with characteristic time [Cravens, 1997],

$$\tau \approx \frac{L^2}{\pi^2 D_m} \tag{1.2}$$

where L is the dynamo characteristic length.

For the Earth (L $\approx$ 3,000 km and $D_m \approx 2$ m^{2}s^{-1}), the magnetic diffusion time τ is 10,000 years; while for Jupiter (L $\approx$ 0.8 R_J, $R_J = 71323$ km, and $D_m \approx 5$ - 50 m^{2}s^{-1}) it is between 200,000 and 2,000,000 years. In both cases, τ is too short regarding the age of the solar system, and thus of the planets [Grodent, 2019].

Therefore, to maintain a magnetic field, the induction equation shows that the velocity of the conductive fluid can not be zero, and thus the convection term dominates. This convective motion produces some currents which create a magnetic field. This is the dynamo mechanism that creates the magnetic field of some planets such as the Earth, Jupiter, and Saturn [Grodent, 2019].

The induction equation suggests that the dynamo effect depends on the magnetic Reynolds number, which defines the relationship between the convection and diffusion processes [Cravens, 1997],

$$R_m = \frac{uB/L}{B/(\mu_0 \sigma L^2)} = \frac{uL}{D_m} \tag{1.3}$$

A dynamo requires the fast rotation of a conductive layer ($R_m \geq 10-100$). In the case of Jupiter, it is the metallic hydrogen. According to Connerney et al. [2018], the possible depth of the Jovian dynamo surface is near ≈ 0.85 R_J.

The *magnetosphere* is the region around a planet where its magnetic field is predominant with respect to all the other forces [Khurana et al., 2004]. Three elements are necessary to create a magnetosphere: a strong planetary magnetic field to counter the solar wind, a source of magnetospheric plasma, and a source of energy to fuel the system [Khurana et al., 2004].

Every object in the solar system is influenced by the *solar wind* emitted from the Sun at a supersonic speed. The interaction of this fast solar wind with the magnetic field of a planet creates a *bow shock*. Behind it, the solar wind flows slower in the *magnetosheath*, the region between the bow shock and the magnetopause. The *magnetopause* is the boundary where the planetary magnetic pressure and the solar wind dynamic pressure are balanced [Bagenal, 2013]. In the magnetopause, strong currents flow around [Khurana et al., 2004].

The planetary magnetic pressure and the solar wind dynamic pressure are defined by [Cravens, 1997],

$$p_{magn} = \frac{B^2}{2\mu_0} \qquad p_{dyn} = \rho_{sw} u_{sw}^2 \tag{1.4}$$

where ρ_{sw} and u_{sw} are the density and the velocity of the solar wind.

Near the planet, the magnetic field can be approximated by a dipole [Cravens, 1997],

$$B = \frac{\mu_0}{4\pi} \frac{m}{r^3} \sqrt{1 + 3sin^2\lambda} \tag{1.5}$$

where m is the magnetic moment, r is the distance to the center of the dipole, and λ is the magnetic latitude.

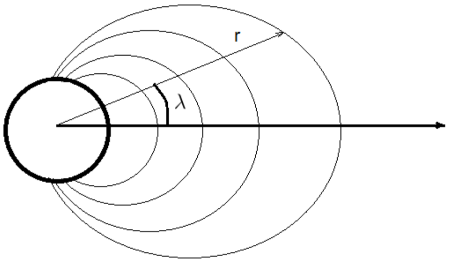

Figure 1.2. Dipolar magnetic field lines. The horizontal line is the magnetic plane.

On the equator, $\lambda = 0$,

$$B_{eq} = \frac{\mu_0}{4\pi}\frac{m}{R_{eq}^3} \tag{1.6}$$

Thus,

$$B = B_{eq}\left(\frac{R_{eq}}{r}\right)^3 \tag{1.7}$$

At the magnetopause, $p_{magn} = p_{dyn}$,

$$\frac{B^2}{2\mu_0} = \rho_{sw}u_{sw}^2 \tag{1.8}$$

Using equations 1.7 and 1.8, the position of the dayside magnetopause is therefore,

$$\frac{r_{mp}}{R_{eq}} = \frac{B_{eq}^{1/3}}{(2\mu_0\rho_{sw}u_{sw}^2)^{1/6}} \tag{1.9}$$

However, the magnetic field created by the magnetopause current has to be taken into account. Consequently, the total magnetic field at the magnetopause is twice the dipolar magnetic field [Grodent, 2019],

$$\frac{r_{mp}}{R_{eq}} = \frac{(2B_{eq})^{1/3}}{(2\mu_0\rho_{sw}u_{sw}^2)^{1/6}} \tag{1.10}$$

For the Earth, the theoretical position of the dayside magnetopause is 10 R$_E$ (where R$_E$ is the radius of the Earth), what fits with the observations (8-12 R$_E$). For Jupiter, the theoretical value is 42 R$_J$, while observations show that this distance varies between 50 and 100 R$_J$. The difference between the theory and the observations lies in the fact that the magnetosphere of Jupiter is mainly controlled by internal processes (Jupiter's fast rotation) and its important internal source of plasma, namely from the Io's volcanism. On the contrary, the magnetosphere of the Earth is controlled by the solar wind, which explains why the theory matches the observations [Grodent, 2019].

On the nightside, there is the *magnetotail*, that can spread over thousands of R$_J$ (See Figure 1.3) [Khurana et al., 2004].

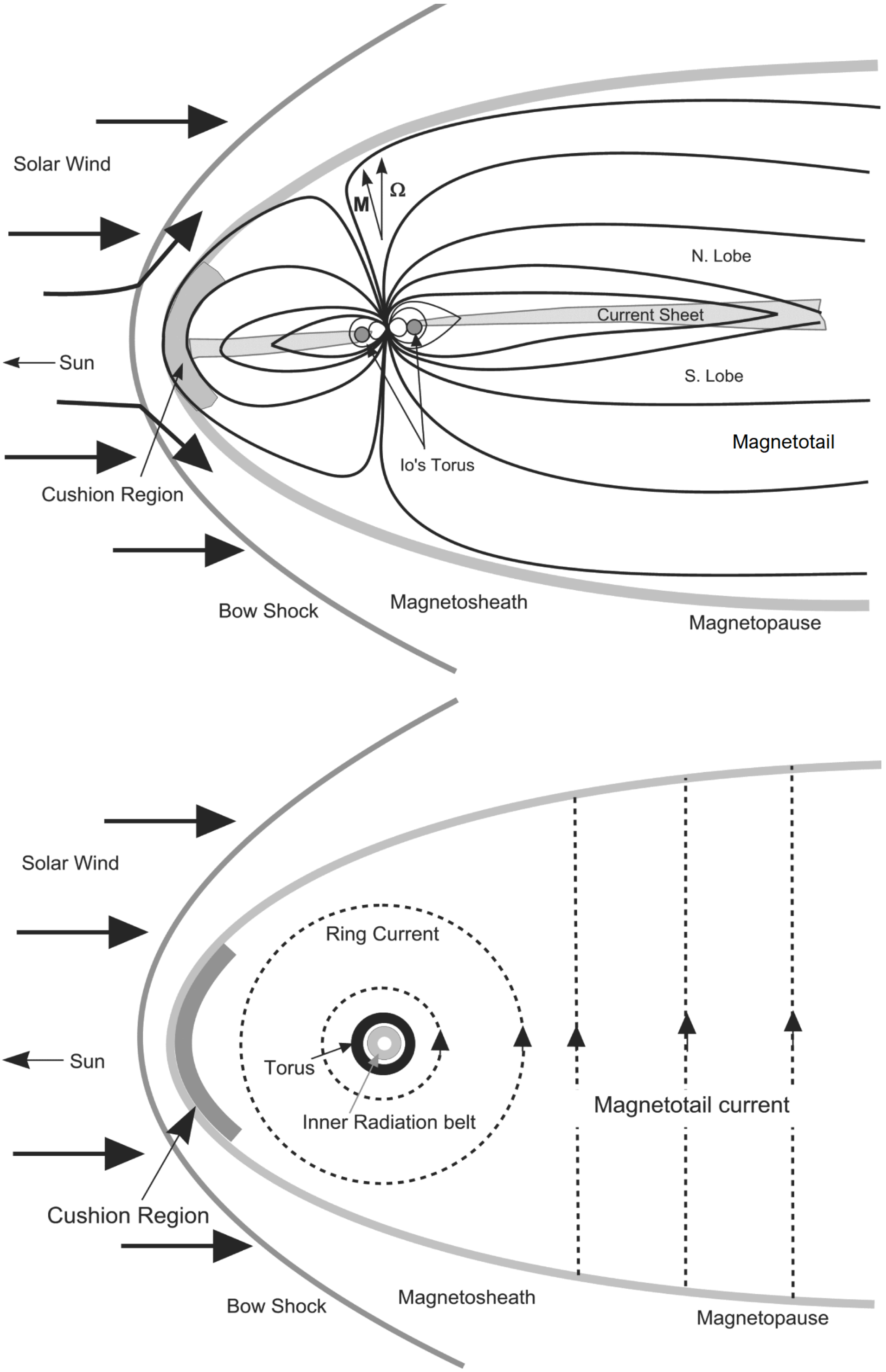

Figure 1.3. Magnetosphere of Jupiter. In the top figure the noon-midnight meridian is shown while the equatorial cross section is shown in the bottom figure. Source: [Khurana et al., 2004].

Jupiter's magnetosphere is separated into three regions: inner magnetosphere (< 10 R$_J$), middle magnetosphere (10-40 R$_J$), and outer magnetosphere (> 40 R$_J$) [Khurana et al., 2004].

Plasma is produced in the **inner magnetosphere**, where the orbits of Io (at 5.9 R$_J$) and Europa (at 9.4 R$_J$) are found. These moons create a plasma torus around Jupiter where neutrals are ionised [Badman et al., 2014]. The main contribution of plasma comes from the volcanic moon Io. The plasma diffuses outwards due to instabilities produced by the centrifugal force. Since charged particles moving across the magnetic field are affected by the Lorentz force ($\mathbf{F}$ = q$\mathbf{v} \times \mathbf{B}$), they will mainly follow the field lines [Khurana et al., 2004]. The moons interact with the magnetic field of the planet producing the auroral footprints. The footprints of Io, Europa, and Ganymede are distinguishable, while the footprint of Callisto is thought to be hidden in the main emission. These footprints appear as spots and trails (features 6, 7, and 8 of Figure 1.5) [Badman et al., 2014].

In the **middle magnetosphere**, as the plasma angular velocity decreases with the radial distance because the conservation of the angular momentum, the plasma corotation with Jupiter's magnetosphere breaks down. The field-aligned currents (FAC) accelerate electrons into the Jovian ionosphere and produce aurorae in this region. In order to retain the plasma against the centrifugal and thermal pressure forces, the magnetic field becomes extended [Khurana et al., 2004]. The magnetic field is therefore deviated from a dipole configuration [Badman et al., 2014].

On the dayside, the **outer magnetosphere** is crushed by the solar wind, but, depending on the intensity of the solar wind dynamic pressure, the magnetopause location may be between 50 R$_J$ and 100 R$_J$. On the nightside, the magnetotail current system appears and it joins the magnetodisc current to the magnetopause currents. This current forms the current sheet and creates a long magnetotail of more than 7,000 R$_J$ that reaches Saturn's orbit [Khurana et al., 2004]. When the current sheet is very thin, reconnection can occur and a plasmoid is released downtail (see Figure 1.4). The reconnected field line goes back towards the planet [Vasyliunas, 1983; Cowley et al., 2003]. In the middle and outer magnetosphere the main contribution to the magnetic field does not come from the internal dynamo field, as in the inner magnetosphere, but from the electric currents lying in the current sheet [Grodent et al., 2008b].

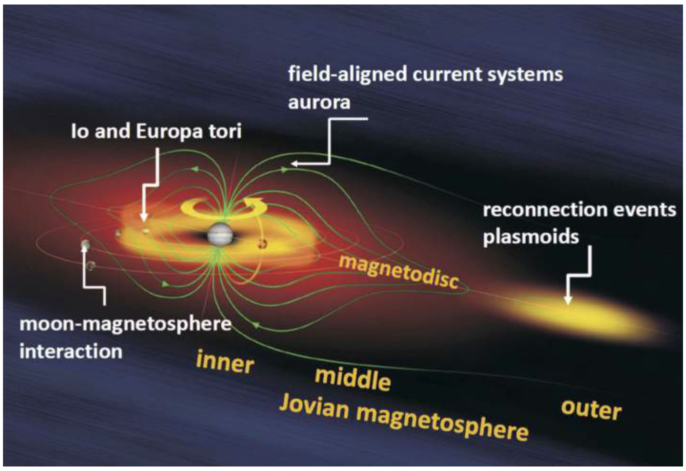

Figure 1.4. Regions of the magnetosphere of Jupiter [Badman et al., 2014].

1.4 The northern Jovian UV auroral emissions

The Jovian magnetic field rotates faster than the moons around Jupiter. This differential rotation of conducting bodies in a magnetic field creates current systems along the magnetic field lines, and thus connects the moons to the Jovian ionosphere. Due to the corotation with the magnetic field, the plasma from the iogenic torus escapes and populates the magnetosphere [Grodent et al., 2008a]. Auroral emissions are the result of inelastic collisions between the neutrals (H_2, H) of the Jovian atmosphere and the energetic electrons of the magnetosphere that precipitate in the ionosphere along the magnetic field lines. These electrons can lose their energy through the ionization, dissociation, and excitation of H_2. Secondary electrons can be produced by ionization, which is the most efficient process. It is possible for the secondary electrons to interact with H_2 molecules again. Even if ionization is more probable than excitation, any electron with an energy above the excitation limit ($\approx$ 10 eV) could produce a UV photon. Nevertheless, the excitation cross section maximises in the 20-160 eV range, primary and secondary electrons colliding with H_2 molecules therefore produce auroral UV photons. The de-excitation of the excited hydrogen molecules produce the emission of UV photons. The electronic interactions continue deeper in the atmosphere until the primary and secondary electrons are thermalised into the surrounding atmosphere. However, dissociative excitation produces around 99% of the auroral UV emission of Jupiter [Grodent, 2014].

In this study, the ultraviolet northern auroral emissions have been studied, as they are easy to obtain thanks to the UV camera, Space Telescope Imaging Spectrograph (STIS), on-board the Hubble Space Telescope (HST). On the other hand, the auroral UV emission is not the only one produced by Jupiter. Its aurorae also shine in other wavelength ranges: radio, infrared, visible, and X-Ray [Grodent, 2014].

The UV aurora of Jupiter consists of four main components: the main emission (ME), emissions equatorward of the ME, emissions poleward of the ME, and the footprints of the Galilean satellites. This classification is made regarding the locations in the ionosphere, and they are originated in different regions of the magnetosphere [Grodent et al., 2018]. In Figure 1.5, the typical ingredients of Jupiter's northern aurora are detailed. The studied region corresponds to the polar active region (feature 9 in Figure 1.5) according to Grodent [2014]. This present study is focused on the region which is associated with the polar active region since nothing has been published so far. It has been identified as Jupiter's auroral bridge since it connects the main emission (feature 1) and the polar region (see Figure 1.6). Only the main emission and the polar region are going to be analysed as they are the regions of interest for this study, where the bridge connecting these two areas appears.

1.4.1 The main emission

The width of the main auroral emission varies between $\approx$100-500 km. The dawn region forms a narrow and continuous arc, whilst it is usually broader at dusk. Nevertheless, the main emission is not continuous as it breaks down in the pre-noon portion [Grodent, 2014]. The power emitted by the main emission contributes to around one third of the total emitted power of the aurora in the UV. The other two thirds are equally emitted by the poleward emissions and the equatorward emissions of the

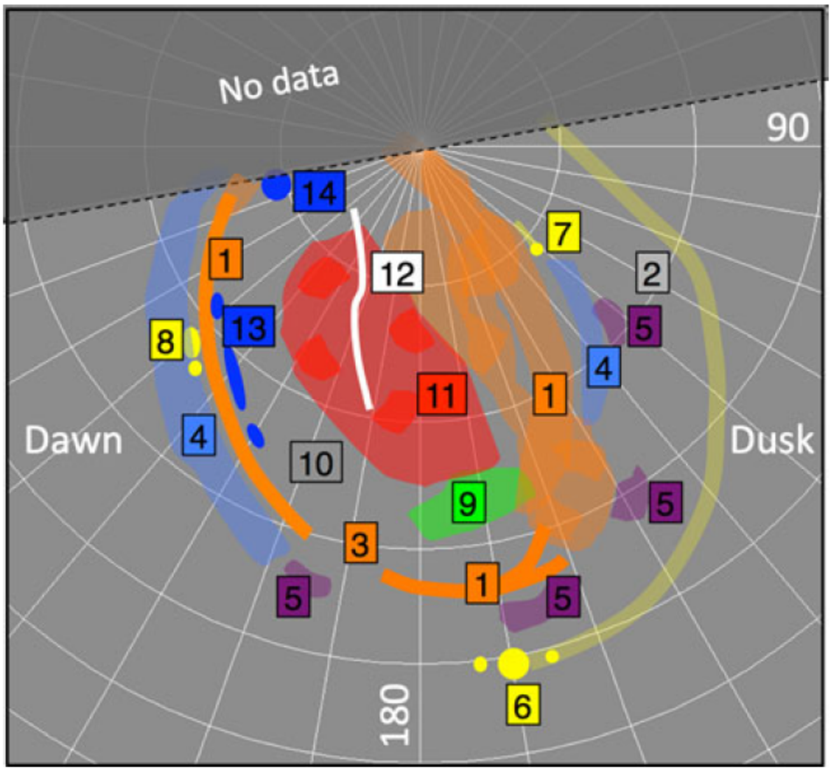

Figure 1.5. Far Ultraviolet (FUV) components of the northern aurora of Jupiter identified by Grodent [2014]. Feature 1 represents the Main Emission (ME); feature 2, the kink region; feature 3, the discontinuity of the ME; feature 4, the secondary emissions; feature 5 shows the signatures of injections; features 6, 7 and 8 indicate respectively the Io, Europa and Ganymede footprints and tails (except for Ganymede); feature 9 represents the polar active region, which contains the polar flares and the arc-like feature, described by Grodent et al. [2003b]; feature 10 shows the polar dark region; feature 11, the polar swirl region; feature 12, the polar auroral filament; feature 13, the dawn spots and arcs; and feature 14, the midnight spot [Grodent, 2014].

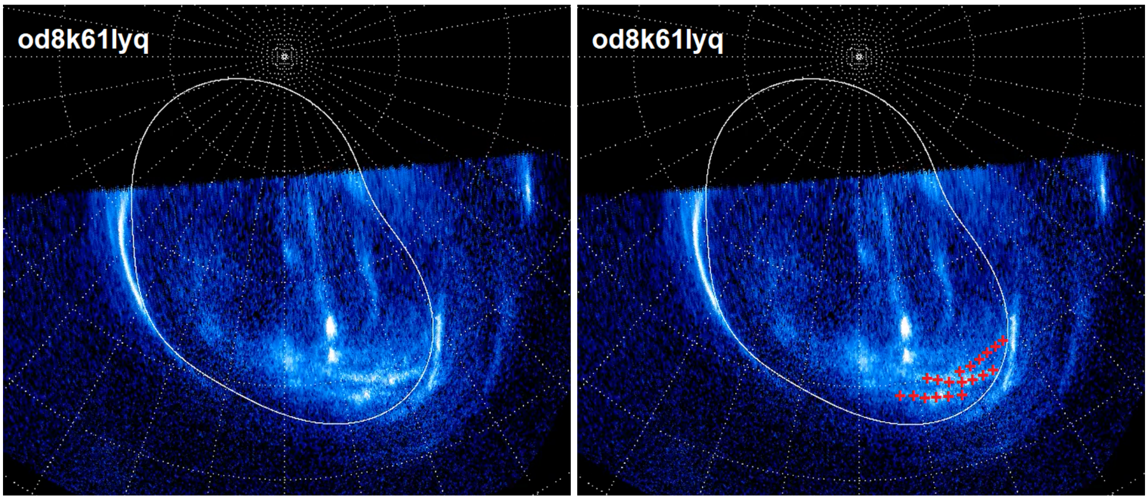

Figure 1.6. Illustration of one of the cases analysed in this study. The auroral bridge corresponds to the emission highlighted by the red crosses on the right panel. This structure matches with the feature 9 of Figure 1.5.

ME [Grodent et al., 2018]. The width and intensity of the main emission can vary. On the one hand, when the magnetosphere is compressed by the solar dynamic pressure, the ME is thinner and more intense, principally on the dawn sector. On the other hand, when the dynamic pressure is weaker, the main emission is broader and its intensity decreases [Nichols et al., 2017]. The upper region (night side) is not accessible to Earth orbit telescopes like the HST [Grodent, 2014].

The simplest models suggest that the main emission is created by the magnetosphere-ionosphere coupling current system which is produced by the corotation breakdown. Because of the conservation of the angular momentum, when the equatorial plasma diffuses outwards, its angular velocity slows down, resulting in the corotation breakdown. In order to accelerate the magnetospheric plasma and to try to conserve the corotation, a radial current is created, and consequently a $\vec{J} \times \vec{B}$ force appears in the plasma sheet. This force is produced by the ion-neutral collision that occurs at the Pedersen layer of the ionosphere [Grodent, 2014]. Nevertheless, these results do not match the observations, and new models are therefore being developed.

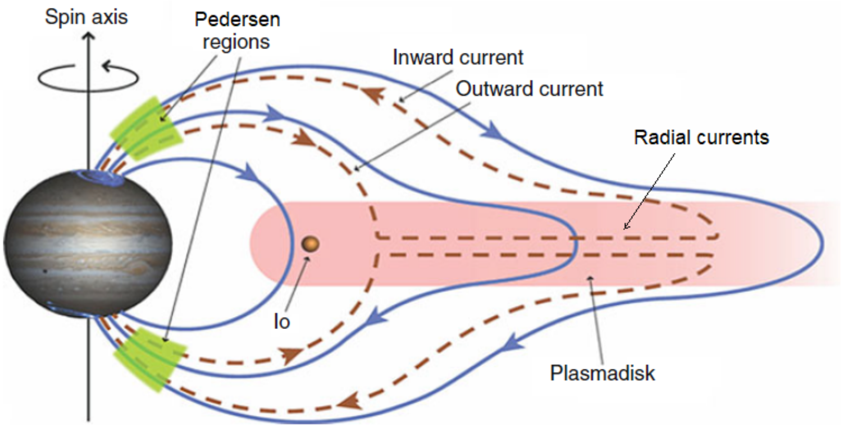

Figure 1.7. Meridional view of the magnetosphere of Jupiter. The Pedersen region is represented in green and the FAC (inward and outward currents) and radial currents are shown in red. The solid blue lines represent the magnetic field lines and the red region is the plasma from Io. [Bagenal, 2013].

As the circuit is closed, field-aligned currents, or Birkeland currents appear, flowing from the ionosphere to the equator in the inner section, and returning towards the ionosphere in the outer section of the system (see Figure 1.7). The electrons diving into the atmosphere of Jupiter lose their energy through collisions with the atmospheric neutrals. Thus, some of this energy is radiated in the UV domain producing the main emission [Grodent, 2014].

According to Radioti et al. [2008], the discontinuity that appears in the main emission (feature 3 in Figure 1.5) could originate from the reduced and inverted field-aligned currents in this region.

There is another important region in the main emission. This is the kink region (feature 2 in Figure 1.5) located between the 80° and 150° System III meridians, where the main emission is distorted. This distortion is due to an anomaly in the surface magnetic field, as suggested by Grodent et al. [2008a] and confirmed by the Juno mission [Connerney et al., 2018].

1.4.2 The polar emissions

These emissions are related to the outer magnetosphere dynamics and they seem to be influenced by the solar wind. The northern polar emissions can be classified in three regions: the active, dark, and swirl regions (features 9, 10, and 11 in Figure 1.5) [Grodent, 2014].

Grodent et al. [2003b] identified two kinds of features in the active region: the polar flares and the arc-like feature. The last one is referred to as Jupiter's auroral bridge, as it connects the main emission and the polar flares. As shown in Figure 1.5, this region is located poleward of the main emission between the noon and the dusk areas. So far, this auroral bridge has received very little attention, which is why it is being considered in the present study.

A more complete study was necessary as there have been several interpretations of this region. In the study of Waite Jr. et al. [2001], they suggested that the polar bright spots of the active region could be produced by an increase in the solar wind dynamic pressure which trouble the outer magnetosphere. Nichols et al. [2017] defined two active regions poleward of the main emission, the Dusk Active Region (DAR) and the Noon Active Region (NAR). They observed that the last region presents pulsating emissions forming arcs poleward of the main emission in any condition of the magnetosphere, compressed or expanded. Therefore, according to this description and its location in the ionosphere, the auroral bridge analysed in this study corresponds to the NAR. Moreover, Grodent et al. [2003b] observed that the arc-like feature moved equatorward when the CML increased, and Bonfond et al. [2011] observed a periodicity in the occurrence of the polar flares of two to three minutes.

1.5 Observing Jupiter: Missions

An effective way to study a planet is to approach it and make in situ measurements. Eight spacecraft have been able to get close to Jupiter and cross its magnetosphere.

In December 1973, Pioneer 10 was the first spacecraft that visited Jupiter. This mission confirmed the strong Jovian magnetic field and its huge magnetosphere. In December 1974, Pioneer 11 arrived at Jupiter at the closest trajectory, 1.6 R_J. This close approach allowed scientists to create a good description of the internal magnetic field [Khurana et al., 2004].

In 1977, the two Voyager spacecraft were launched. Voyager 1 flew by Jupiter in March 1979, while Voyager 2 arrived in July 1979. Thanks to this mission, the dense iogenic plasma torus and the equatorial current sheet were discovered [Khurana et al., 2004].

In February 1992, Ulysses used Jupiter in order to conduct a gravity assist to explore the interplanetary medium. Ulysses could thus explore the dusk high latitude region of Jupiter, unbeknownst before this date [Khurana et al., 2004].

In October 1989, the Galileo spacecraft was launched and it orbited Jupiter from December 1995 until September 2003, when the spacecraft plunged into the atmosphere finishing its long journey. This mission provided a significant quantity of data that is still being used today. In the Jovian system, Galileo explored the atmosphere of Jupiter, its rings, and magnetosphere, as well as the

Galilean moons. Amongst other findings, Galileo discovered a liquid water ocean beneath Europa's ice shell and observed the volcanic activity of Io [Bagenal et al., 2004; NASA, c].

In December 2000, Cassini flew by Jupiter in order to reach Saturn and its moon Titan [Bagenal et al., 2004].

New Horizons visited Jupiter in February 2007 using its gravity so as to increase its speed to continue its journey toward Pluto and the Kuiper Belt. During its flight over Jupiter, New Horizons collected some information about the atmosphere and the magnetosphere of Jupiter as well as some images of its satellites and aurorae [NASA, b].

Finally, the Juno mission is the last, and the most important, mission to Jupiter as it sets out to determine how much water is in Jupiter's atmosphere as well as measuring its composition, temperature, and cloud motions [Bagenal et al., 2014]. One of the most important goals of this mission is to combine remote sensing of Jovian aurorae with the first in situ measurements of the particles and magnetic and gravity fields carried out by Juno. Moreover, the UVS (Ultraviolet Spectrograph) and JIRAM (Jovian Infrared Auroral Mapper) instruments on board Juno are measuring the auroral emissions [Bolton et al., 2017a]. Juno is also providing incredible images of Jupiter's poles and moons. It was launched in August 2011 and it arrived at Jupiter in July 2016, when it began orbiting Jupiter on a trajectory of 53 days. At perijove, Juno flies over Jupiter at 3,500 km above the cloud tops. On the opposite side of the orbit, the spacecraft reaches distances of 100 R_J, tracing a very elliptical trajectory [Grodent et al., 2018].

Jupiter is also continuously observed from Earth's orbit. In fact, for this study, UV images taken by the Space Telescope Imaging Spectrograph (STIS) on board the Hubble Space Telescope (HST) have been used. The Hubble Space Telescope was launched in April 1990 and it is still operating. HST was launched from the Kennedy Space Centre in Cape Canaveral, Florida. It was located in an orbit at 534 km above the Earth's surface. Originally, there were four instruments on board: the High Speed Photometer (HSP), the Wide Field/Planetary Camera (WFPC), the Faint Object Camera (FOC), and the Goddard High Resolution Spectrograph (GHRS). Nevertheless, the telescope has been repaired four times by astronauts who also added new instruments. Currently, there are six instruments on board HST:

- The Wide Field Camera 3 (WFC3) which is used to obtain the most spectacular images in ultraviolet, visible and infrared wavelengths.
- The Cosmic Origins Spectrograph (COS) is used to split UV radiation.
- The Advanced Camera for Surveys (ACS) is used to get visible-light images of deep space.
- The Near Infrared Camera and Multi-Object Spectrometer (NICMOS) operated from 1997 to 1999, and from 2002 to 2008. NICMOS was sensitive to IR light and it provided information about distant galaxies, planets, star formations and solar systems, which are hidden by interstellar gas.
- The Space Telescope Imaging Spectrograph (STIS) is used to obtain the images for this study. Its characteristics will be explained in next chapter.

- Hubble carries three Fine Guidance Sensors (FGS) in order to help the telescope to point in the right direction.

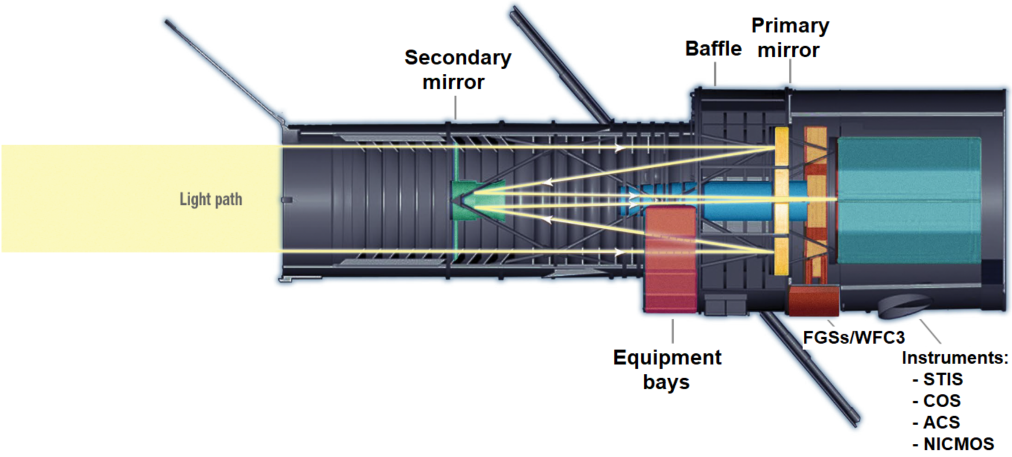

Figure 1.8. Hubble Space Telescope internal configuration. The light path is shown, as well as the location of the instruments on board. Source: [NASA, a]

The HST is a Cassegrain reflector telescope, where incoming light is reflected in a primary concave mirror towards a smaller secondary mirror. The secondary mirror reflects light to the primary mirror through a hole in its centre to the focal plane, where the scientific instruments are located (Figure 1.8) [NASA, a].

As well as these instruments, the HST can receive and send information to a set of satellites thanks to four antennae. The satellites then communicate with Earth. There are solar arrays that get solar energy and transform it into electricity to power HST. Some of the energy is stored in batteries to be used when the telescope is below the Earth's shadow. Finally, the on-board computers control the instruments and the pointing system [NASA, a].

Chapter 2

Methods

In this chapter, the methods and equipment used for this study are explained. The ultraviolet images analysed were obtained by the Space Telescope Imaging Spectrograph (STIS) instrument on board the Hubble Space Telescope (HST). The first task consisted in classifying the events and choosing three clear cases where Jupiter's auroral bridge is observed. For each case, about 250 images were analysed. The pixels where this emission appears were selected in order to know the emitted power of this region and their location in the ionosphere. Thereafter, the power emitted was used to estimate the percentage of the total power emitted by the aurora and the periodicity of this emission using a Lomb-Scargle periodogram. In order to know their position in the magnetosphere of Jupiter, some mapping models were used. Finally, as each model has varied calculations and limitations, the projected points show some differences in location. To outline these differences, some plots were carried out.

2.1 Observations with the STIS instrument

For this study, the UV auroral emissions of the northern hemisphere of Jupiter were analysed. These images were obtained during the HST observing campaign 14634 (from November 2016 to July 2018). The images had been previously processed and then provided by the Laboratory for Planetary and Atmospheric Physics (LPAP) of the University of Liège as movies. Each movie contained a HST visit. These visits lasted ≈ 41 minutes and collected about 250 images, that is one image every 10 seconds. The images were obtained by the STIS instrument on-board HST. STIS was installed on HST in February 1997 during the Second Servicing Mission (SM2). It was in operation until 2004, when it suffered an electronic failure. Fortunately, STIS was fixed in 2009 during the Forth Servicing Mission (SM4). Currently, it is still operating [NASA, e]. STIS reveals the temperature, chemical composition, density, and motion of celestial objects. As this instrument measures from the FUV to the NIR, it can analyse black holes, the atmospheres of other planetary systems, and the intergalactic medium [NASA, a]. STIS contains three large-format (1024×1024 pixel) detectors: one CCD camera that operates in the optical and NIR (200-1,100 nm) and covers a 52" × 52" field of view (FOV), and two Multi-Anode Microchannel Array (MAMA). One of them operates in the NUV (160 to 310 nm), and the other one in the FUV (115 to 170 nm). The MAMA detectors are photon-counting devices that cover a 25" × 25" FOV [NASA, e].

The STIS instrument provided the first high resolution UV images of the aurorae of Jupiter and allowed the study of Jupiter's polar atmosphere, its composition, its temperature and the precipitating particles that produce the aurora. At the distance of Jupiter, STIS can reach a spatial resolution of 100 km and a FOV of 25" × 25" that catches approximately one-fourth of the Jovian disk [Grodent, 2014; Grodent et al., 2003a].

2.2 Image processing

All auroral images were reduced from the initial data files using routines developed and tested at the LPAP. This procedure converts the counts obtained by STIS into physical parameters such as the brightness, precipitated power, and radiated power. The background brightness was then subtracted in order to remove the sunlight reflected on the planet and only keep the auroral emissions [Gustin et al., 2012]. The background subtraction requires generating a model planetary disk simulating the reflected sunlight on the planet [Bonfond et al., 2011]. The model planetary disk is obtained by determining the centre position of Jupiter by a limb-fitting procedure since just one-fourth of the Jovian disk is captured by STIS' field of view [Bonfond et al., 2009]. After that, a latitude and a longitude are assigned to each pixel of the original image, allowing to do projections of the images onto a polar plane. This polar projection allows us to easily identify the auroral features that are corotating with the planet [Grodent et al., 2003a]. In Figure 2.1, one can see that the crosses are distorted near the limb which means that the projection accuracy decreases in this region. These projections are made at a height of 400 km, above the 1-bar pressure level, defined as the surface. They take the equatorial and polar radii of Jupiter into account as well as the inclination of the planet and the HST-Jupiter distance. Nevertheless, the vertical spread of the auroral emission is neglected [Grodent et al., 2003a].

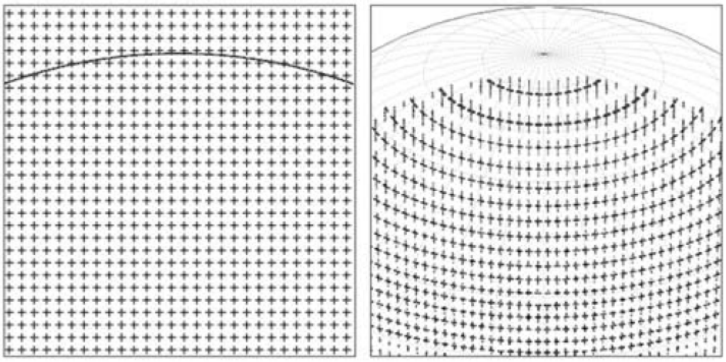

Figure 2.1. Left: original image. The curve shows the section of the planetary limb inside the STIS' field of view. The equidistant crosses represent the emission. Right: image after the projection procedure [Grodent et al., 2003a].

2.3 Classification of the events

After analysing all the images, the bridge could be observed in most cases. Nevertheless, in some cases like on 21^{st} of May 2017 (file rootname of the STIS observation: od8k0cgpq), no auroral bridge was visible. Afterwards, three visits or cases were selected for this study. The criterion was to choose three distinctive events with different appearances in order to consider typical cases where the auroral bridge shines. Some details of these three events are listed in Table 2.1 below.

In order to have in situ information, this HST data set was coordinated with the Juno mission. The cases considered in this study correspond to the data obtained during Juno's orbits 3 to 7.

Index	Rootname	Juno's orbit	HST time (dd/mm/yyyy)	CML start	Family
k24	od8k24ioq	3	03/12/2016	162.7527	Unclassified
k57	od8k57itq	5	19/03/2017	146.2975	X
k61	od8k61lyq	5	22/03/2017	163.6913	i

Table 2.1. List of various parameters characterising the three cases analysed in this study. In the last column, the family classification made by Grodent et al. [2018] (explained below) is indicated.

In the unpublished paper of Yao et al., they present several observations of the Jovian aurorae carried out by HST and Hisaki space telescope and the measurements of magnetic field, particles and radio waves by Juno. In Figure 2.2, the processes of loading and unloading are presented. These magnetic loading and unloading processes, evident in the active periods (Figure 2.2 (a)), represent the accumulation and release of magnetic energy in the magnetosphere. Figure 2.2 (a) shows the magnetic field measured by Juno during its fifth orbit around Jupiter. This orbit corresponds to the events k57 and k61, observed by HST. One can observe that case k57 corresponds to the beginning of an unloading process (release of energy) [Yao et al.]. In case k57, the energy stored during the previous days was released from 19^{th} to 20^{th} March 2017. The case k61 took place on 22^{nd} March 2017. Nevertheless, in Figure 2.2, there is no data shown after this day, but the tendency is the same as in case k57, i.e. an unloading event.

In Figure 2.2 (b), the magnetic strength of case k24 is shown. In this case, the magnetic field is weaker than in the previous two cases, which corresponds to the broader and weaker main emission. This event took place on 3^{rd} December 2016, during the third orbit of Juno. Comparing Figures 2.2 (b) and (c), it could correspond to a quiet event, similar to the one of Juno's orbit 7. The three events presented in Table 2.2 took place during orbit 7.

However, the study of Yao et al. is too recent and it would be necessary to carry out more research to make an accurate correlation between the occurrence of the auroral bridge and the loading/unloading processes.

Nevertheless, one can sort these events according to the classification made by Grodent et al. [2018]. In their study, they defined six auroral morphology families in order to specify the variations of the auroral emissions: quiet (Q), unsettled (U), narrow (N), moderate injections (i), strong injections (I), and external perturbation (X). These families can be related to the state of the magne-

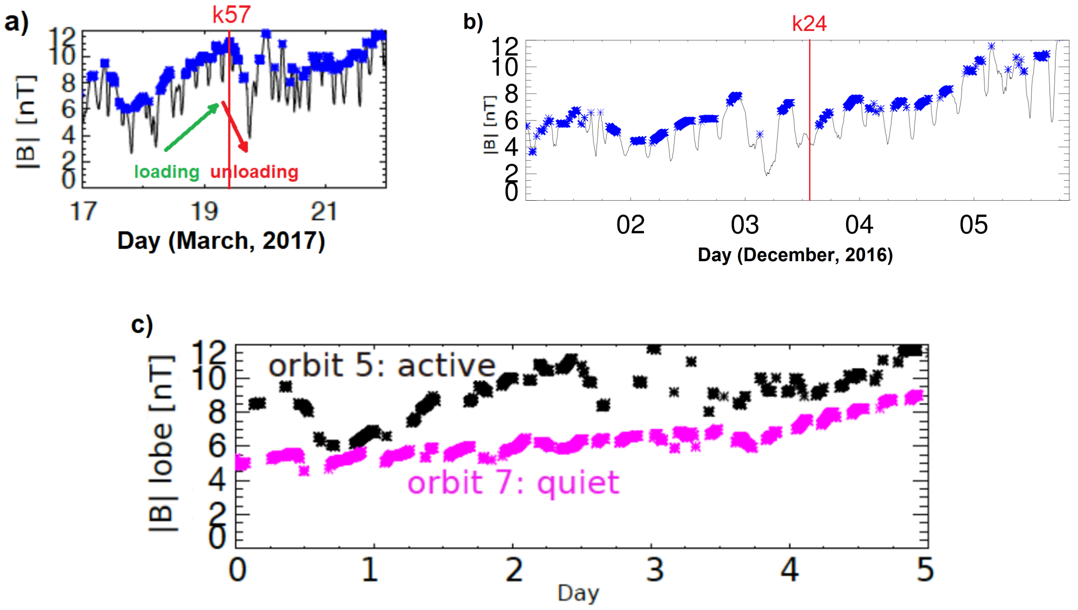

Figure 2.2. Magnetic field measured by Juno during different orbits corresponding to the HST cases analysed in this document. (a) Juno's orbit 5: HST events k57 and k61. (b) Juno's orbit 3: HST event k24. The vertical red lines indicate the dates of the events analysed. (c) Comparison between an active (compression by the solar wind dynamic pressure) and a quiet (no compression) event. Moreover, the three cases where no auroral bridge was observed (presented in Table 2.2) belong to orbit 7. Adapted from Yao et al..

tosphere, which is affected by internal and external elements like the quantity of iogenic plasma and the solar wind dynamic pressure [Grodent et al., 2018].

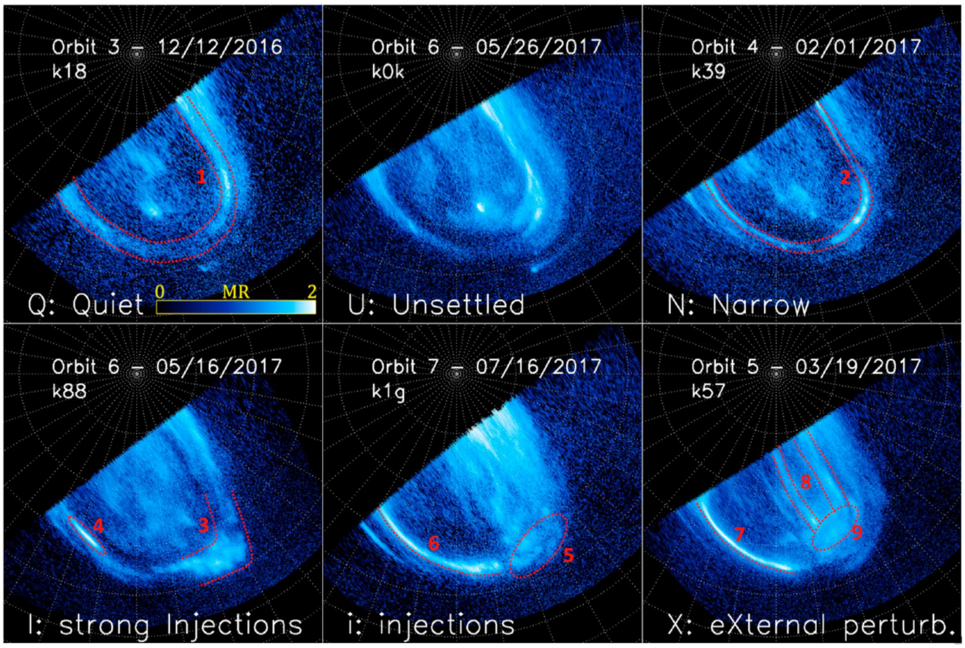

Figure 2.3. The six auroral families of Jupiter's UV northern aurora, defined by Grodent et al. [2018], are shown for different Juno orbits and HST visits.

The Q family comprises the morphologies where the radiated power is very low and the main emission (ME) is thus broad and faint. The morphology of the N family is a very narrow ME and it has a mean power. The U family is an intermediate family between the two previous ones. The i family presents moderate injection signatures and a continuous main emission. The I family comprises the same morphology as the i family, but the brightness of the equatorward subregion is higher and it presents a corner-shaped feature (3 in Figure 2.3). Moreover, the dawnside main emission appears disrupted. Finally, the X family shows a strong and contracted dawnside ME as well as strong poleward arcs parallel to the duskside ME (feature 8) [Grodent et al., 2018]. As shown in Figure 2.3, the auroral bridge (feature 9) is easily identifiable in this morphology group. Grodent et al. [2018] ascribed one index for each family, which reveals the typical power measured in each group. These indexes are: 1 for the family Q, 2 for the family U, 3 for the family N, 4 for the family i, 5 for the family I, and 6 for the family X.

In Table 2.1, the three cases analysed in this study are presented. These three events contained auroral bridges. Nevertheless, they belong to different families as their morphologies and emitted power are different. In Table 2.2, three cases where the auroral bridge was not observed are listed. Below, these six events are going to be described according to Grodent et al. [2018] and Figure 2.4.

Index	Rootname	Juno's orbit	HST time (dd/mm/yyyy)	Family
k0c	od8k0cgpq	7	21/05/2017	N
k0q	od8k0qldq	7	05/07/2017	Q
k0f	od8k0fwuq	7	08/07/2017	Q

Table 2.2. List of three cases where no auroral bridge was observed. In the last column, the family classification made by Grodent et al. [2018] is indicated.

Case k24 must fit the Q family due to its morphology. Nevertheless, the total emitted power is higher regarding the other cases of this family [Grodent et al., 2018]. Because of this uncertainty, this case was not included in the analysis made by Grodent et al. [2018]. Analysing the images of the previous days (k22 and k23), it has been observed that no auroral bridge appeared. These cases happened during the third orbit of Juno around Jupiter. In fact, k24 shows the lowest emitted power of the three events analysed with an observed auroral bridge (Table 2.1). Since there is no more information about k24, one can check the surface subtended by the ME the previous day (k23). In table S1 of the supporting information for Grodent et al. [2018], this area is $0.915 \cdot 10^9$ km^2, which is evidence of an expanded magnetosphere.

Case k57 belongs to Juno's orbit 5 and it is present in Figures 2.3 (bottom right) and 2.4 (centre right). According to Grodent et al. [2018], k57 corresponds to the X family as it shows a strong and contracted dawnside ME. In most of the cases of this family, the bright ME appears joined to strong polar emissions in the dusk side, as in k57. In this case, the auroral bridge is very powerful and there are strong arcs parallel to the duskside ME. In table S1 of the supporting information for Grodent et al. [2018], the area subtended by the main emission is $0.796 \cdot 10^9$ km^2, which indicates a magnetosphere more compressed than in the previous case, although it is not very compressed.

Case k61 also belongs to Juno's orbit 5. This event took place three days after k57 and its family is different. According to Grodent et al. [2018], it corresponds to family i. In this case, the auroral bridge appears to have travelled towards the noon sector regarding the two previous cases. Three bridges are recognisable, instead of two as in the other two cases (see Figure 2.5). In table S1 of the supporting information for Grodent et al. [2018], the area subtended by the main emission is $1.017 \cdot 10^9$ km^2, which indicates that the magnetosphere is less compressed than in case k57.

Nevertheless, although the area taken up by the main emission is about 10^9 km^2 in these three cases, corresponding to a not very compressed magnetosphere, Yao et al. suggest that the visits k57 and k61 happened during a solar wind compression. The case k57 shows a smaller ME area than the other two cases, probably corresponding to this assumption. In conclusion, the Jovian magnetosphere might not have been sufficiently compressed to show measurable effects in the aurora, but these effects were probably detected by Juno's in situ measurements. There is therefore an uncertainty about the compression state of the magnetosphere.

The last 3 cases, shown in Table 2.2, are the three cases without an observed auroral bridge. These events took place during Juno's orbit 7 (Figure 2.2 (c)). According to Grodent et al. [2018], k0c belongs to the N family, while k0q and k0f match the Q family (see Figure 2.4 down). k0c emits an average power and shows a narrow ME, while k0q and k0f show very faint emissions and a broader ME. The surface taken up by the ME in these three cases is about 10^9 km^2, which indicates an expanded magnetosphere. Therefore, these last three events correspond to a low solar wind dynamic pressure (Figure 2.2 (c)) and, consequently, a low interplanetary medium activity [Grodent et al., 2018].

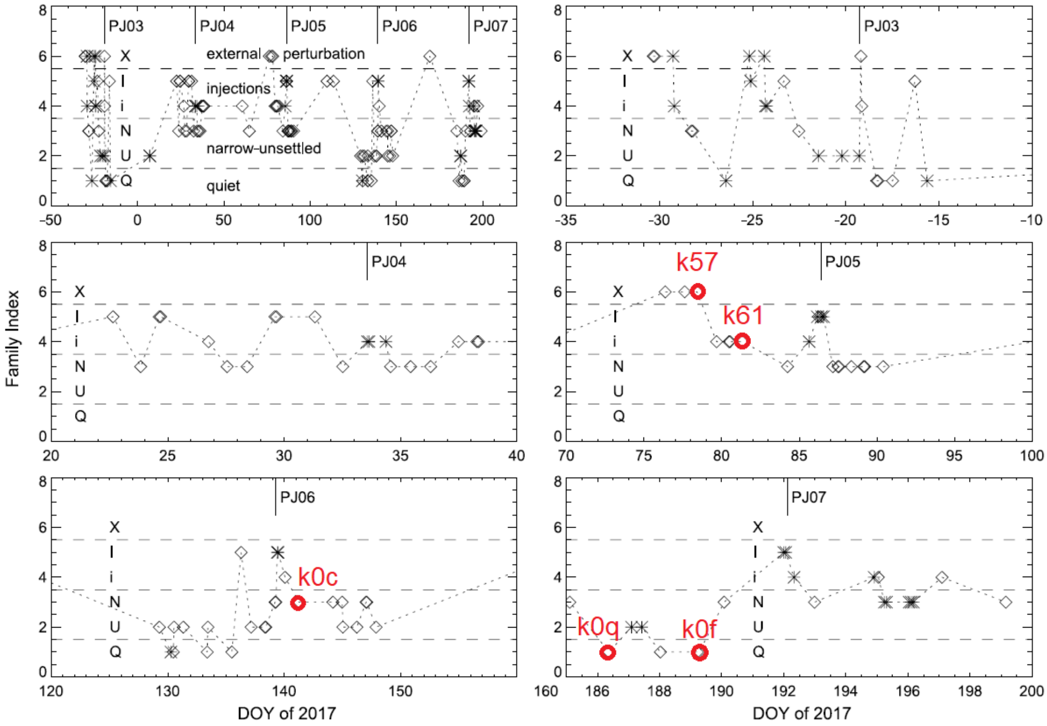

Figure 2.4. Evolution of the morphology of the northern and southern Jovian aurorae over Juno orbits 3 to 7. On the vertical axis, the six families indexes are indicated. On the horizontal axis, the days of year (DOY) 2017 are shown. The red dots represent the cases analysed in this study, except k24. Adapted from Grodent et al. [2018].

2.4 Images analysis: Coordinates and power of the auroral bridge

The position of Jupiter's auroral bridge and the power emitted by this feature were obtained from the images described above. The routines used have been written in IDL (Interactive Data Language). Some of the routines were provided by LPAP and, then, they were adapted for this study. Other routines were uniquely created for this analysis. They are presented in the Appendix B. For this part, the routine `irene.script` was used.

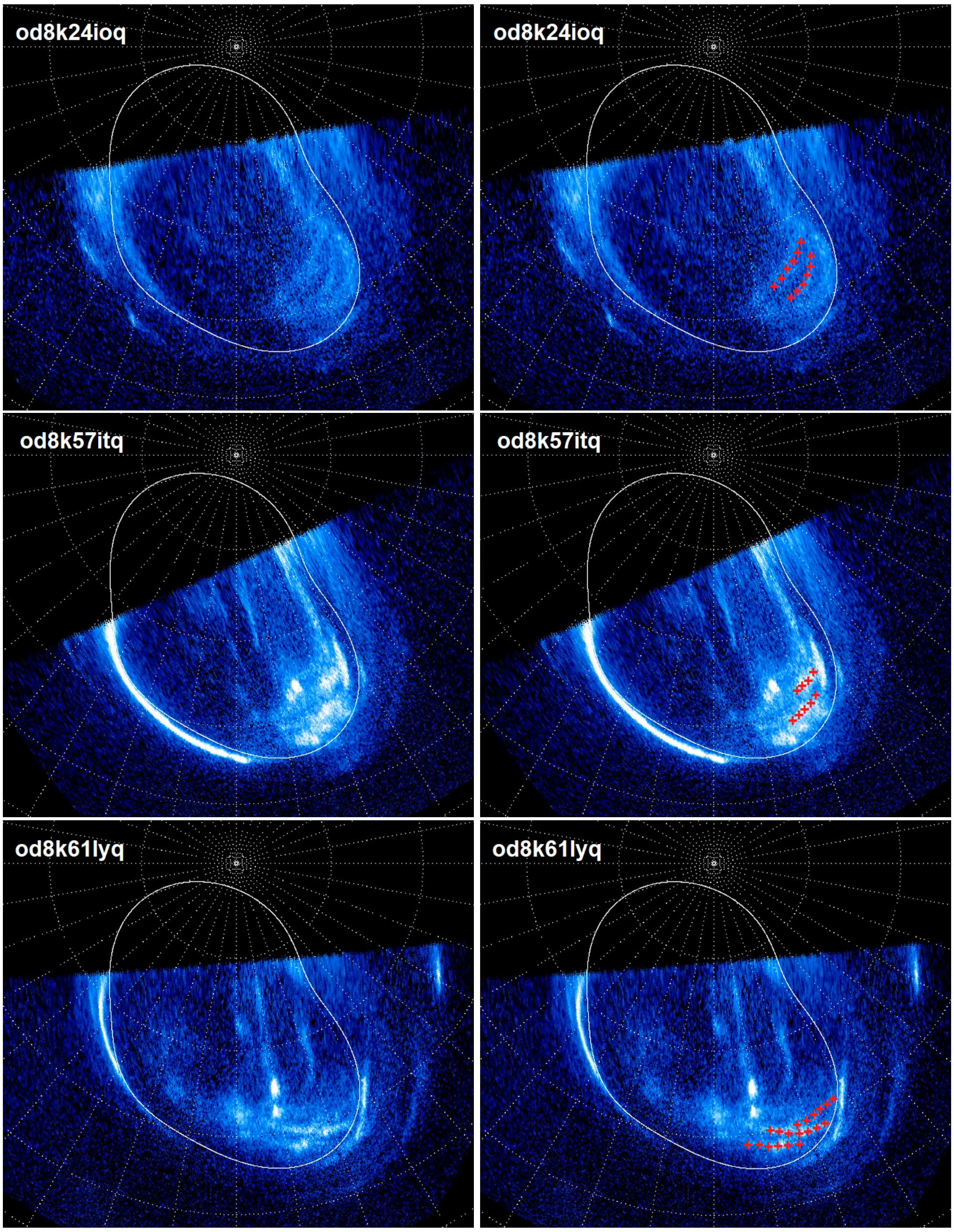

Figure 2.5. Images of the three cases where Jupiter's auroral bridge appears. On the left side, the original images are shown. On the right side, the red crosses indicate the auroral bridge. In cases k24 and k57, two bridges were observed, while in k61, a third one appeared.

One of the main points of this study is to know the position of Jupiter's auroral bridge in the ionosphere in order to know if it corotates with the planet. Afterwards, these coordinates were projected to the magnetosphere of Jupiter using several models which will be explained in the next section.

Another important parameter is the power radiated (in W) by this feature. The power was retrieved to analyse variations in intensity and periodicity of these emissions. The emitted power evokes the quantity of energy received from the magnetosphere at any one time. The emitted power is affected by three processes: the conversion from STIS counts per second to radiated power, the background subtraction, and the correction of the viewing geometry [Grodent et al., 2018]. The conversion from STIS counts per second to radiated power is affected by the amount of methane absorption [Gustin et al., 2012]. The inaccuracies in the background subtraction are constant over a HST visit ($\approx$ 41 minutes). Finally, the viewing geometry uncertainty is due to the fact that HST does not capture the whole auroral region [Grodent et al., 2018]. Nevertheless, only the images where the auroral bridge is completely visible were selected. The measured power emitted by this region is thus not affected by this uncertainty.

In order to obtain these parameters (location in the ionosphere and emitted power) the routines `traceoval.pro` and `rdpix.pro` presented in `irene.script` were used. The first routine (`traceoval.pro`) allowed us to obtain the coordinates (latitude and longitude in local time) when clicking on an image pixel (like the red crosses showed in Figure 2.5). The RDPIX procedure displays the X and Y positions and the pixel value at the cursor. According to the parameters defined in `irene.script`, the pixel value displayed corresponds to the power (in W) of the pixel selected. Therefore, the points where the auroral bridge appeared in the ionosphere were selected by clicking on the corresponding pixels. The locations of these points (longitude, latitude) were obtained for each CML thanks to the `traceoval.pro` routine. In order to obtain the emitted power, the area of interest was selected and the RDPIX procedure provided the power emitted by each pixel. Finally, all these values were added together in order to estimate the total power emitted by the studied region. The power was retrieved from the original images and not from their polar projections, since the projection procedure stretches the pixels and thus does not conserve photometry. An important limitation is that in this region the polar flares also appear. This could modify the real power emitted exclusively by the auroral bridge, so one must be very careful when selecting the region of interest in order to avoid most of the polar flares.

2.5 Mapping from the ionosphere to the magnetosphere

The differential rotation of the moons (conducting bodies) around Jupiter create current systems along the magnetic field, connecting the moons to the Jovian ionosphere [Bonfond et al., 2017]. Charged particles (principally electrons) entering the Jovian atmosphere interact with the atmospheric neutrals in the ionosphere, generating the auroral emissions. In order to discover the source of the auroral emissions, some models were used. Some of them trace field lines connecting a point in the ionosphere to a point in the magnetosphere, using static 3D models of Jupiter's internal magnetic field. There is another model, developed by Vogt et al. [2011], which uses the flux equivalence between the ionosphere and the equatorial magnetosphere. In this section, all these models are going to be described.

2.5.1 Tracing field lines from a global field model

These models use the observed auroral footprints of one or more of the Galilean moons and their location in the magnetosphere. The orbits of the Galilean moons are well known: Io at 5.9 R_J, Europa at 9.4 R_J, and Ganymede at 15 R_J. The footprint of Callisto was not observed. It is thought that Callisto orbits at the distance mapping to the main emission, preventing the observation of its footprint [Grodent, 2014].

There are several models that employ field line tracing: VIP4, GAM, JRM09, VIPAL, and Khurana. For this study, only GAM, JRM09, and Khurana models were used. However, all the models will be briefly explained in order to understand the evolution of this method.

VIP4 model

This model was developed by Connerney et al. [1998] to calculate the field parameters. Voyager magnetometer data, Io footprint observations, and Pioneer 11 magnetometer were used and thus gave it its name. Nevertheless, Ulysses magnetometer data was also used. This model correctly fits the Io footprint contour, except in the kink region in the northern hemisphere [Vogt et al., 2015].

GAM model

In order to improve the correlation between the VIP4 model and the observed satellite contours in the kink region, GAM (Grodent Anomaly Model) was developed by Grodent et al. [2008a]. The modification consisted of adding a magnetic anomaly. This anomaly is produced by a weakening of the surface magnetic field in this region. A magnetic dipole located near the surface was therefore included. Nevertheless, only the northern hemisphere can be modeled using GAM. Grodent et al. [2008a] selected the central location of the footprints of Io, Europa and Ganymede, unlike VIP4 which uses only the Io position [Grodent et al., 2008a].

VIPAL model

This model was developed by Hess et al. [2011]. VIPAL is an upgrade from VIP4. It adds the magnetic anomaly described in Grodent et al. [2008a] and includes longitudinal constraints on the mapping of the Io footprint, ignored by VIP4. The surface magnetic field strength predicted by VIPAL correlates better with Jovian radio emission than the previous models [Hess et al., 2011].

JRM09 model

JRM09 (Juno Reference Model through Perijove 9) was developed by Connerney et al. [2018]. This new model of the Jovian magnetic field was created from observations of the magnetic field obtained by Juno during the first nine polar orbits around Jupiter. The first nine orbits provided the first global coverage of the magnetic field of the planet. Thanks to Juno, this model has improved the prediction of the magnetic field at close distances to the planet and it will help to plan future operations of the Juno mission [Connerney et al., 2018].

Khurana model

The unpublished Khurana magnetic field model [Khurana] is a model based on data from the Galileo spacecraft. It was written in Fortran 77/90 in 2003 by Krishan Khurana and then translated into IDL by Adam Shinn. This model calculates the magnetic field of a tilted and distorted magnetosphere [Khurana]. The Khurana model normally uses VIP4 as the internal field, but it can also use JRM09.

2.5.2 Flux equivalence mapping: the Vogt et al., 2011 model

In the inner magnetosphere, the main contribution to the magnetic field comes from the internal Jovian dynamo field, however, beyond the orbit of Ganymede, an external contribution associated with the electric currents flowing around Jupiter in the current sheet appears [Grodent et al., 2008b]. Consequently, Jovian magnetic field global models are generally inaccurate beyond 30 R_J, which complicates linking polar auroral features to source regions in the middle and the outer magnetosphere. In order to improve the mapping results made by tracing field lines, Vogt et al. [2011] developed a model that uses a flux equivalence calculation. This model consists of conserving the magnetic flux between an equatorial region in the magnetosphere and a region in the ionosphere. The calculation starts in the orbit of Ganymede (15 R_J). The model traces field lines from this orbit in the magnetosphere (at the equator) to the ionosphere, where Ganymede's footprint location is known. Afterwards, it calculates the flux through a region in the magnetosphere and links it to the flux through the ionosphere (at higher latitudes than the Ganymede's one) until both fluxes are equivalent (see Figure 2.6) [Vogt et al., 2015].

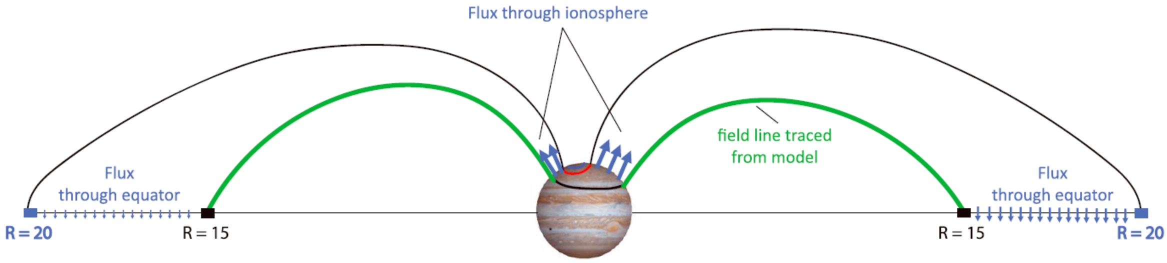

Figure 2.6. Meridional view of the flux equivalence mapping for a magnetospheric equatorial region between 15 R_J and 20 R_J. The green field line represents the Ganymede projection from the magnetosphere to the ionosphere, obtained from a global field model. The black line is obtained thanks to the equivalent flux through an equatorial region in the magnetosphere and through a region in the ionosphere. Not to scale [Vogt et al., 2011; 2015].

Nevertheless, this flux equivalence model requires an internal field model to locate the auroral reference contour of Ganymede and to calculate the radial field through the ionosphere [Vogt et al., 2015]. These models can be GAM, JRM09, VIP4, and VIPAL, but not Khurana. The first two ones were used for this study.

In this mapping model, Vogt et al. [2011] used all data provided by the Galileo mission, under all solar wind conditions. This data was used to fit the equatorial magnetic field used for the calculation of the flux. The model corresponds thus to an average solar wind condition, which corresponds to an expanded magnetosphere since expansions seem more common than compressions.

2.5.3 Mapping function 2019

This function (`mapping_function2019_june.pro`) was written by Marissa Vogt, currently at Boston University, in IDL language and it was last updated in June 2019. It allows us to map the locations which correspond to the auroral bridge in the ionosphere towards the magnetosphere. These points can be projected by tracing field lines from a global field model or by using the flux equivalence model described above.

There are several parameters that have to be introduced as inputs of the function [Vogt et al., 2011; 2015]:

- **mapping_type**. It specifies the type of mapping: from the magnetosphere to the ionosphere, or from the ionosphere to the magnetosphere. For this study, the mapping type was done from the northern ionosphere to the magnetosphere.
- **sslong**: the subsolar longitude, expressed in degrees system III left-handed.
- **input_position1 and input_position2**: coordinates in the ionosphere to be mapped to the magnetosphere. Position1 corresponds to the latitude in degrees, and Position2 is the longitude in degrees SIII left-handed.
- **Model**. Here the internal field model is selected.
- **Fieldline_Tracing**. If this option is selected, the mapping will be done by tracing field lines from a global field model, chosen in the previous input (model). On the other hand, if this option is not selected, the Vogt et al. [2011] flux equivalence calculation is run by default. Nevertheless, an internal field model must be selected, as explained above. All the results are pre-calculated.

This function outputs an array of two values, radial distance in R_J, and local time (LT) in hours (0-24) [Vogt et al., 2011; 2015].

In some cases, the point is not mapped for several reasons: if the ionospheric location is equatorward of the Ganymede footprint (distance < 15 R_J in the magnetosphere), if the point is outside 95 R_J, beyond the magnetopause, or if the program has an error [Vogt et al., 2011; 2015].

In order to map by tracing field lines, VIP4, VIPAL, and JRM09 only map up to $\approx$ 85 R_J; while GAM maps up to $\approx$ 65 R_J [Vogt et al., 2011; 2015].

To undertake the mapping, the routine `ionosph_to_msph_ipc` (see Appendix B) was used. After the mapping, all the magnetospheric points were plotted in order to verify the source region in the magnetosphere (routine `plot_data_mgnp_ipc`). Several plots were created in order to show the results for each model. In order to better understand the location in the magnetosphere of these points, two magnetopauses were added to the plots, the dayside magnetopause of the first one is located at 60 R_J (compressed magnetosphere) and the second one at 90 R_J (expanded magnetosphere) [Joy et al., 2002; Vogt et al., 2011]. To do that, the dynamic pressures selected have been 0.37 nPa for the compressed magnetospere, and 0.044 nPa for the expanded magnetosphere, as proposed by Joy et al. [2002]. Since five locations in the magnetosphere (one for each model) were obtained for each point in the ionosphere, the mean location and the standard deviation were calculated in order to estimate only one location and to compare the models. These calculations and plots are described in the routines `mean_stdev_flag_models_ipc` and `plot_error_bars_ipc` developed for this study. All the results and discussion will be detailed in Chapter 3.

Chapter 3

Results and discussion

The location as well as the periodicity at which the auroral bridge pulses and the power emitted by this structure were analysed. Thanks to the mapping models, the location (radial distance and local time) in the equatorial plane of the magnetosphere was obtained. In order to understand the origin of this structure, all these observations were compared with the results of the MHD model simulation of Fukazawa et al. [2006]. The results of the analysis carried out will be presented in this chapter.

3.1 Mapping from the ionosphere to the magnetosphere

The field line tracing and the flux equivalence calculation described in Chapter 2 were executed using the GAM, JRM09 and Khurana internal field models. The mapping results are shown from Figure 3.1 to Figure 3.3. The central dot symbolises Jupiter. Several contours centered at Jupiter have been depicted in order to indicate the radial distances (in R_J). These contours are drawn every 20 R_J. Local Time Noon (12 LT) can be found at the bottom of the figure, dawn (6 LT) on the left side, midnight (0 LT) at the top, and dusk (18 LT) on the right side. Moreover, two locations of the magnetopause have been outlined, the inner one corresponds to a strongly compressed magnetosphere (dayside magnetopause at 60 R_J) and the outer one, to the expanded magnetosphere (dayside magnetopause at 90 R_J) [Joy et al., 2002; Vogt et al., 2011]. The dynamic pressure used to obtain the compressed magnetopause was 0.37 nPa, while for the expanded magnetopause it was P_d = 0.044 nPa. This second position of the magnetopause represents a more compressed magnetosphere than the one assumed by the mapping model written by Vogt et al. [2011]. Such model only considers an expanded magnetosphere with P_d = 0.039 nPa. According to Vogt et al. [2011], the solar wind condition taken into account in this model corresponds to an average magnetopause. Since expansions seem more common than compressions, this expanded magnetosphere is relatively close to the average case. Finally, the red dots show the locations obtained in the equatorial plane after mapping each pixel selected in the ionosphere. This pixel selection method was explained in Section 2.4.

Case k24

In the first plot of Figure 3.1, the points were obtained by field line tracing using the GAM model. One can see that the mapped dots stop at 65 R_J, which corresponds to the outer boundary of the GAM model. In this case, all the points can be found inside the compressed magnetopause. In the second plot of Figure 3.1, more points appear and they are mapped inside the expanded magnetopause, which confirms the assumption of the low solar dynamic pressure described in Section 2.3 This situation is also found in the mapping made by the JRM09 (centre) and Khurana (down) models. In the case of the JRM09 field line tracing, the points stop at the limit of the model, 85 R_J.

In local time, the points cover from 11:00 hours to 20:00 hours and, in radial distance, they expand over 30 R_J to 110 R_J, approximately (see Figure 3.1). Even though, the points mapped by each model are different and are in the borders, most of them are found in the same region, between noon and dusk.

Case k57

In this case, the mapped points appear closer to Jupiter for most of the models. Similar to the previous case, one can observe the limitations of GAM (65 R_J) and JRM09 (85 R_J) when the mapping is done by tracing field lines (Figure 3.2 up-left and centre-left). Apart from the GAM model restriction, most of the points are located between the two magnetopauses. As explained in Section 2.3 this case corresponds to a very slightly compressed magnetosphere. Nevertheless, the ME in k57 is the thinnest one of the three analysed cases. This event corresponds thus to a more compressed magnetosphere than in the other two, which explains why about one third of the points are located inside the compressed magnetopause.

Regarding the expansion of the mapped points, this structure covers from 11:00 LT to 20:00 LT and from 20 R_J to 100 R_J (see Figure 3.2). As it is similar to the previous event, it is also found in the region between noon and dusk.

Case k61

In this case, one can again observe the mapping limitations of the GAM and JRM09 models. As shown by the models, the points map out of the compressed magnetopause. Consequently, the magnetosphere was expanded, as explained in Section 2.3. In this case, and in k57, few points map out of the expanded magnetosphere because the dynamic pressure used to plot the magnetopause in this study is different than the one assumed by the Vogt et al. [2011] model.

As shown on Figure 2.5, the auroral bridge does not appear exactly at the same location on the ionosphere as in the previous cases. The points were therefore not found in the same region as in k24 and k57 when mapping to the equatorial plane. In this case, the points cover from 9:00 h to 17:00 h in local time and from 30 R_J to 90 R_J in radial distance (see Figure 3.3). The points in the magnetosphere are thus shifted towards the noon sector.

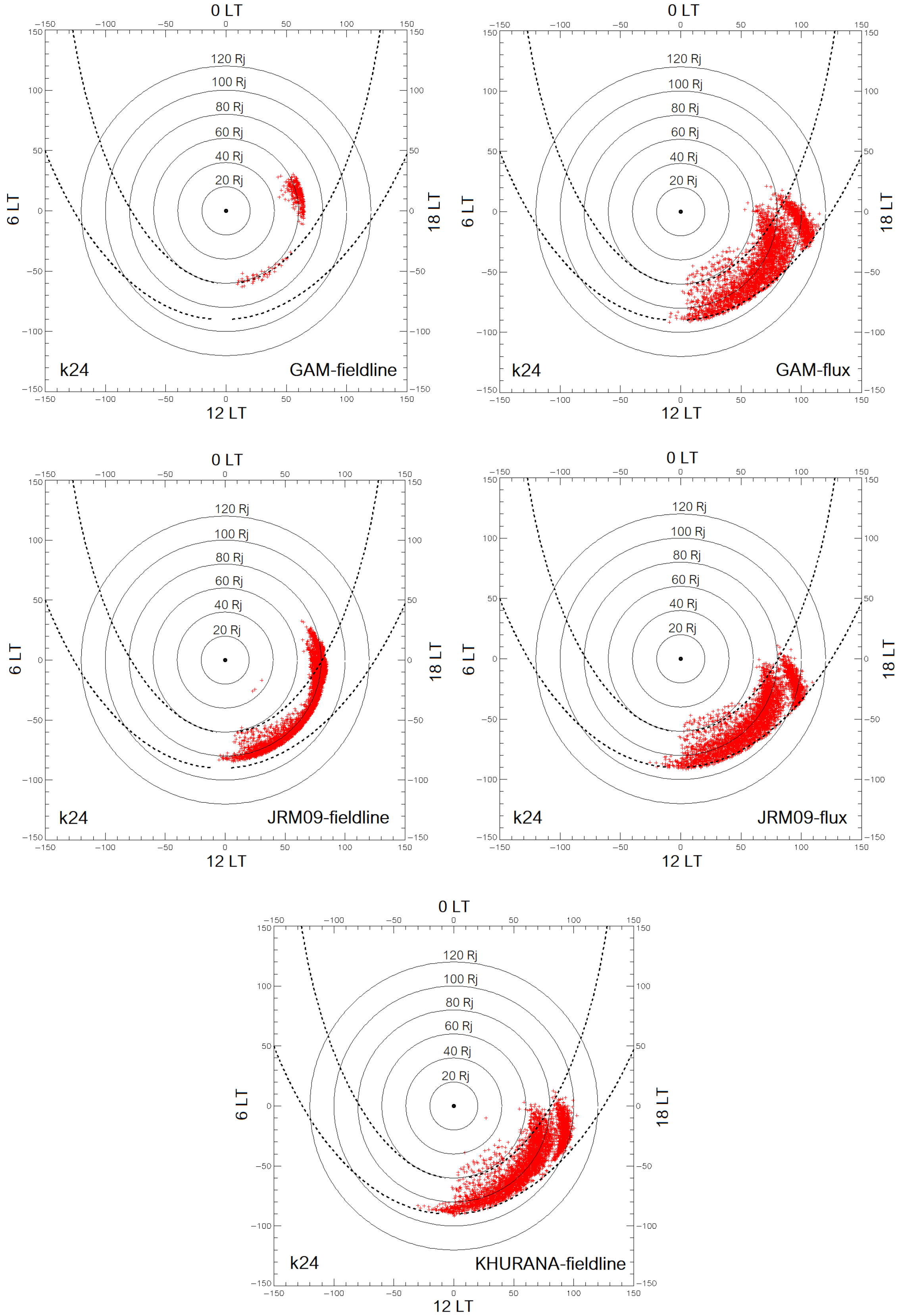

Figure 3.1. Case k24. Results of the mapping from the ionosphere to the magnetosphere (equatorial plane) by field line tracing (left) and by flux equivalence (right) using the GAM model (up) and the JRM09 model (centre) as internal field models. Down, the mapping was done by field line tracing using the Khurana model. The central dot represents Jupiter and the red dots are the projected data. Sun is positioned downwards. The dashed lines indicate probable magnetopause locations for compressed (60 R_J; $P_d = 0.37$ nPa) and expanded (90 R_J; $P_d = 0.044$ nPa) magnetosphere cases.

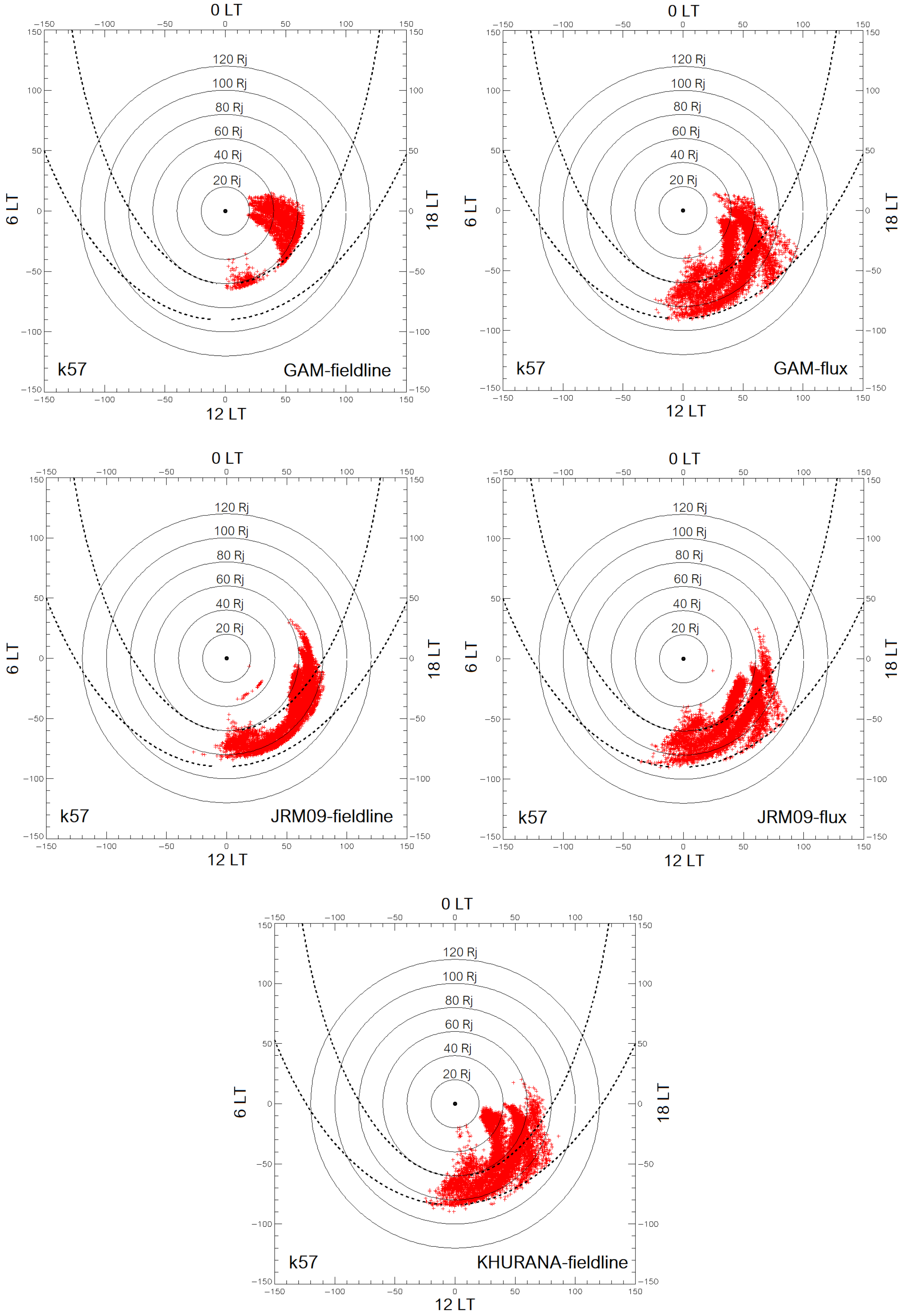

Figure 3.2. Case k57. Results of the mapping from the ionosphere to the magnetosphere (equatorial plane) by field line tracing (left) and by flux equivalence (right) using the GAM model (up) and the JRM09 model (centre) as internal field models. Down, the mapping was done by field line tracing using the Khurana model. The central dot represents Jupiter and the red dots are the projected data. Sun is positioned downwards. The dashed lines indicate probable magnetopause locations for compressed (60 R_J; $P_d = 0.37$ nPa) and expanded (90 R_J; $P_d = 0.044$ nPa) magnetosphere cases.

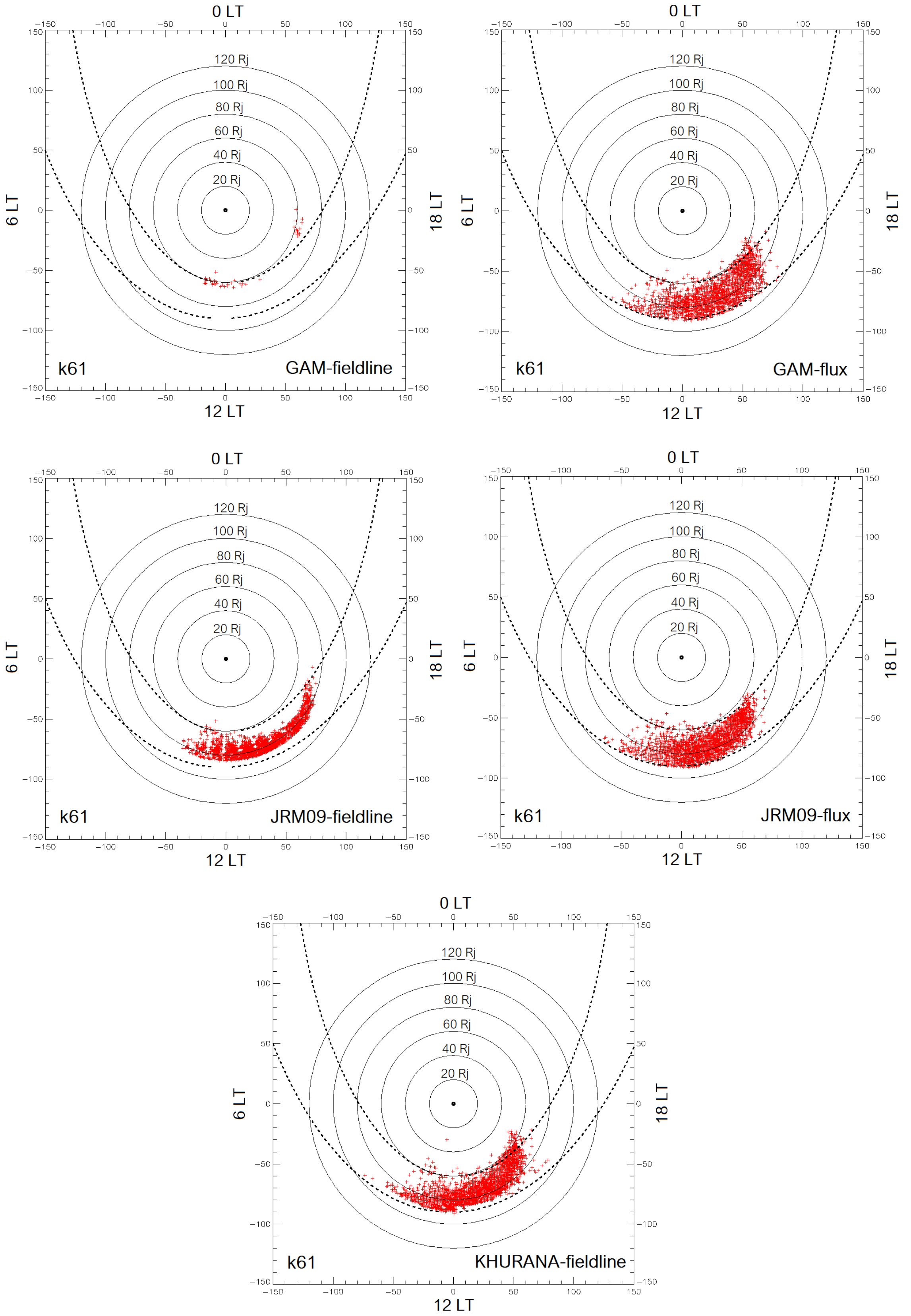

Figure 3.3. Case k61. Results of the mapping from the ionosphere to the magnetosphere (equatorial plane) by field line tracing (left) and by flux equivalence (right) using the GAM model (up) and the JRM09 model (centre) as internal field models. Down, the mapping was done by field line tracing using the Khurana model. The central dot represents Jupiter and the red dots are the projected data. Sun is positioned downwards. The dashed lines indicate probable magnetopause locations for compressed (60 R_J; $P_d = 0.37$ nPa) and expanded (90 R_J; $P_d = 0.044$ nPa) magnetosphere cases.

3.2 Study of the region of interest

In order to estimate the accuracy of the mapping method, the mean and the standard deviation of the positions obtained by the five different calculations were determined. An example of these results is shown on Table 3.1. This table was made using data from the case k24. The first and the second columns show the mean and standard deviation of the radial distance (RD), and the third and the fourth ones indicate the mean and standard deviation of the local time (LT). The last column provides a flag, which was defined as the number of mapping models (0 - 5) that were able to convert an auroral ionospheric location (latitude and longitude at a given CML) into a location in the magnetosphere (LT and RD). It was necessary since some of the mapping models (GAM-fieldline, GAM-flux, JRM09-fieldline, JRM09-flux, Khurana-fieldline) do not map certain points, as explained in Section 2.5.3. The six locations shown in Table 3.1 were selected to illustrate the six possibilities, which are: the five mapping models provided a valid location in the magnetosphere (Flag = 5), four of them provided an answer (Flag = 4), likewise for Flags = 3, 2, and 1. Finally, Flag = 0 corresponds to the case where none of the models could trace this ionospheric point back to the magnetosphere.

mean(RD)	**stdev(RD)**	**mean(LT)**	**stdev(LT)**	**Flag**
83.2	14.3	17.9	0.7	5
94.8	10.3	17.4	0.5	4
86.8	4.6	14.8	0.2	3
97.3	20.4	17.3	0.1	2
84.7	NaN	17.6	NaN	1
NaN	NaN	NaN	NaN	0

Table 3.1. Example table showing how the mean and standard deviation values were obtained for six different locations in the ionosphere. This data corresponds to case k24.

In Figure 3.4, the mean locations (RD and LT) in the magnetosphere are shown. The different colours indicate the flag, i.e., the number of models that were able to carry out the mapping. In case k24, the maximum mean RD is about 108 R_J and the minimum is about 47 R_J. Regarding the local time, the maximum mean LT is 19:00 hours and the minimum is 11:00 h (see Table 3.2). In case k57, the maximum mean radial distance is about 93 R_J, while the minimum is 34 R_J. The maximum mean local time is almost 20:00 h and the minimum is about 11:00 h (see Table 3.3). Finally, in the last case (k61), the maximum mean RD is 91.5 R_J and the minimum is nearly 47 R_J. The maximum mean LT is about 17:00 h and the minimum mean LT is close to 9:00 h (see Table 3.4). Generally, the points are located in the noon-dusk region, as explained in Section 3.1.

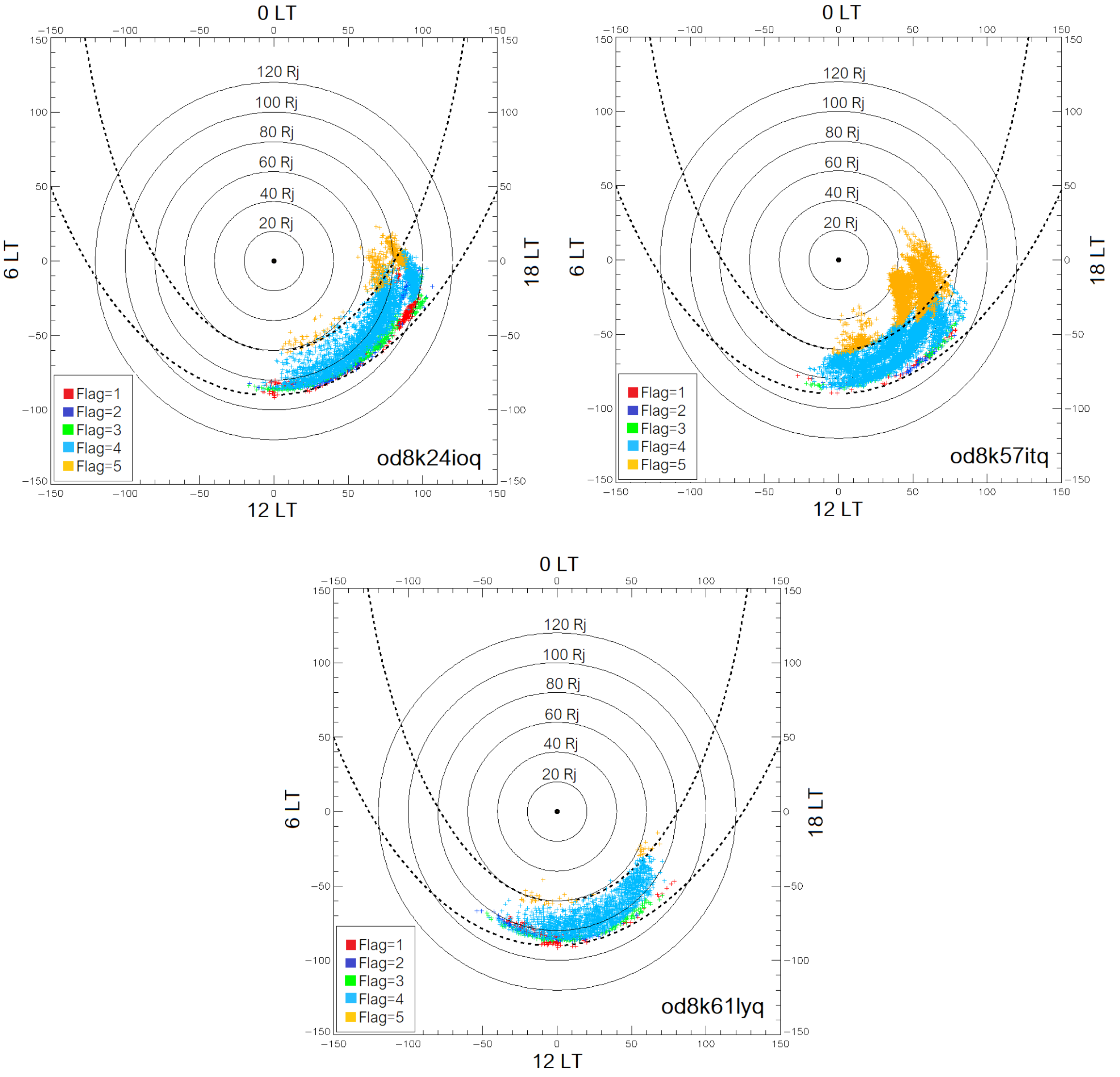

Figure 3.4. Representations of the mean locations (RD and LT) obtained by the five mapping models used in this study. Top left: case k24. Top right: case k57. Bottom: case k61. The flags indicate the number of models that were able to convert an auroral ionospheric location into a location in the magnetosphere. Jupiter is at the centre and the Sun is positioned downwards. The dashed lines indicate probable magnetopause locations for compressed (60 R_J) and expanded (90 R_J) magnetosphere cases.

In order to estimate the accuracy of the mapping models, some representative points were selected to show their mean values and standard deviation, since the large number of points in the magnetosphere did not produce clear graphs. In these graphs (see Figures 3.5, 3.6, and 3.7), the mean locations and the corresponding error bars representing the standard deviation are shown. It can be observed that for each mean location in the magnetosphere, two error bars appear. They represent the standard deviation in both coordinates (RD and LT) for each point of interest. Long bars show a high standard deviation and thus the points obtained by the different mapping models are spread out over a wide range of values. On the contrary, short bars represent a better agreement between the models. Since some of the points of interest are repeated (see tables below), they appear overplotted on these figures.

mean(RD)	stdev(RD)	mean(LT)	stdev(LT)	Flag	Point	Value
107.8	8.3	17.4	0.1	2	max(mean(RD))	107.8
47.3	8.9	14.4	0.2	5	min(mean(RD))	47.3
105.7	3.8	16.8	0.2	2	max(diff(RD))	101.9
80.4	44.8	16.9	0.3	3	min(diff(RD))	35.6
72.4	12.8	19.2	0.7	5	max(mean(LT))	19.2
85.5	5.0	11.2	0.6	3	min(mean(LT))	11.2
98.5	22.5	17.8	0.2	2	max(diff(LT))	17.6
85.4	5.7	11.5	1.1	2	min(diff(LT))	10.4
80.4	44.8	16.9	0.3	3	max(stdev(RD))	44.8
84.2	0.1	13.1	0.7	2	min(stdev(RD))	0.1
86.6	4.0	12.7	1.1	2	max(stdev(LT))	1.1
90.7	2.5	15.0	0.0	2	min(stdev(LT))	0.0

Table 3.2. Points of interest for case k24. On the left side of the table, the mean and standard deviation of the radial distance and the local time are shown for each point as well as the flag indicating the number of models that were able to carry out the mapping. On the right side, the point of interest and its value is indicated.

mean(RD)	stdev(RD)	mean(LT)	stdev(LT)	Flag	Point	Value
93.3	5.8	15.8	0.2	2	max(mean(RD))	93.3
33.8	8.1	13.6	0.2	5	min(mean(RD))	33.8
93.3	5.8	15.8	0.2	2	max(diff(RD))	87.5
45.4	38.8	16.7	0.2	3	min(diff(RD))	6.6
48.2	19.8	19.8	0.3	5	max(mean(LT))	19.8
82.6	NaN	10.7	NaN	1	min(mean(LT))	10.7
45.3	18.9	19.7	0.3	5	max(diff(LT))	19.4
86.6	5.6	11.2	0.8	3	min(diff(LT))	10.4
45.4	38.8	16.7	0.2	3	max(stdev(RD))	38.8
75.3	0.5	11.9	0.3	4	min(stdev(RD))	0.5
36.0	8.5	13.0	1.3	5	max(stdev(LT))	1.3
49.8	6.8	13.3	0.1	5	min(stdev(LT))	0.1

Table 3.3. Points of interest for case k57. On the left side of the table, the mean and standard deviation of the radial distance and the local time are shown for each point as well as the flag indicating the number of models that were able to carry out the mapping. On the right side, the point of interest and its value is indicated.

In Tables 3.2, 3.3, and 3.4, the mean and standard deviation values of the selected points are shown for the three study cases. On the right side of the tables, the point of interest is indicated. These points correspond to the maximum and minimum values of the mean radial distance and local time, as well as the maximum and minimum values of the standard deviation of RD and LT. In order to have more points spread over the studied region, other points were selected. These points correspond to the maximum and minimum difference between the mean and the standard deviation

mean(RD)	stdev(RD)	mean(LT)	stdev(LT)	Flag	Point	Value
91.5	NaN	12.0	NaN	1	max(mean(RD))	91.5
46.8	9.3	11.2	0.2	5	min(mean(RD))	46.8
88.6	3.5	13.2	0.4	2	max(diff(RD))	85.1
46.8	9.3	11.2	0.2	5	min(diff(RD))	37.5
69.0	6.1	17.2	0.6	5	max(mean(LT))	17.2
85.9	12.5	9.4	1.1	2	min(mean(LT))	9.4
65.0	6.0	16.1	0.3	4	max(diff(LT))	15.8
85.9	12.5	9.4	1.1	2	min(diff(LT))	8.3
81.9	13.1	12.5	0.2	2	max(stdev(RD))	13.1
83.9	0.4	12.2	0.8	2	min(stdev(RD))	0.4
85.9	12.5	9.4	1.1	2	max(stdev(LT))	1.1
86.8	3.4	12.7	0.1	5	min(stdev(LT))	0.1

Table 3.4. Points of interest for case k61. On the left side of the table, the mean and standard deviation of the radial distance and the local time are shown for each point as well as the flag indicating the number of models that were able to carry out the mapping. On the right side, the point of interest and its value is indicated.

of RD and LT. For each one of the points of interest, all the parameters are shown on the left side of the tables.

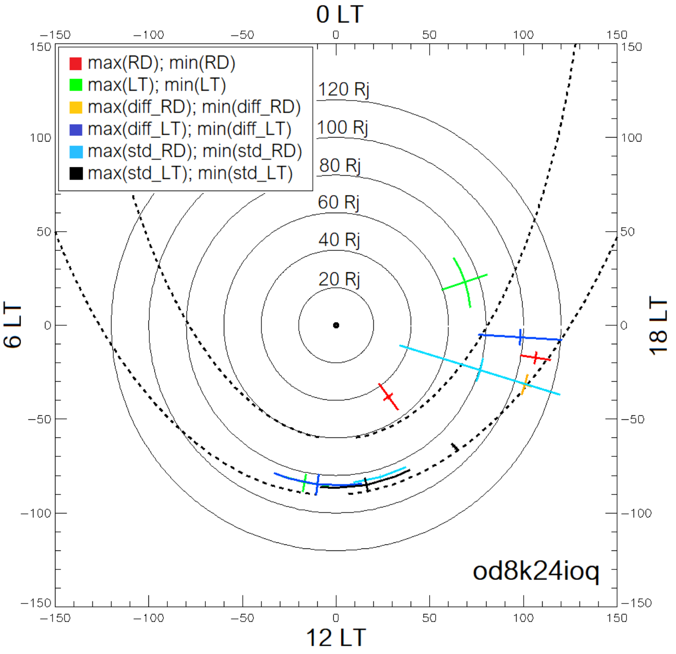

Figure 3.5. Representation of the points of interest and their error bars which depict the standard deviation in both coordinates (RD, LT). These points are described in Table 3.2 for case k24. Each colour indicates the maximum and minimum values of each one of the points. Jupiter is at the centre and the Sun is positioned downwards. The dashed lines indicate probable magnetopause locations for compressed (60 R_J) and expanded (90 R_J) magnetosphere cases.

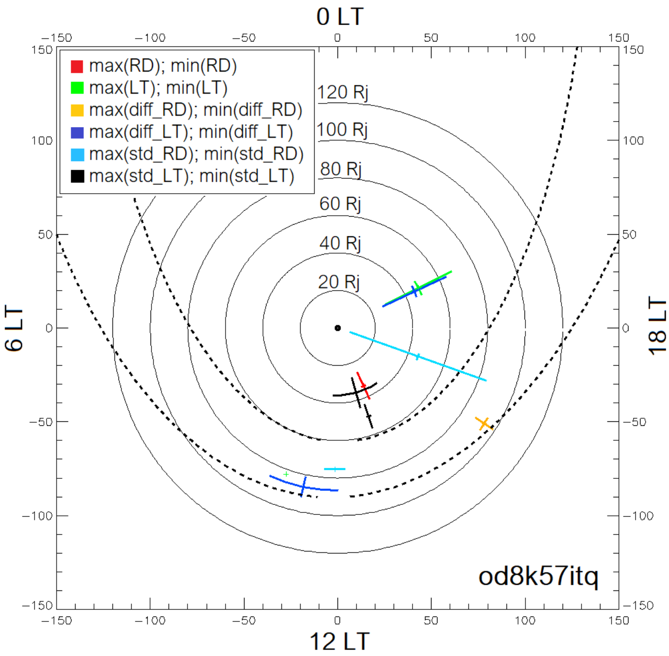

Figure 3.6. Representation of the points of interest and their error bars which depict the standard deviation in both coordinates (RD, LT). These points are described in Table 3.3 for case k57. Each colour indicates the maximum and minimum values of each one of the points. Jupiter is at the centre and the Sun is positioned downwards. The dashed lines indicate probable magnetopause locations for compressed (60 R$_J$) and expanded (90 R$_J$) magnetosphere cases.

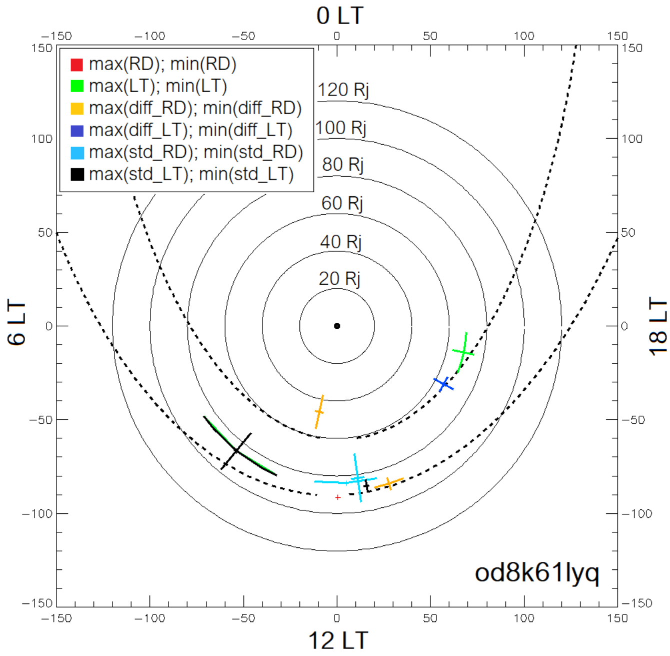

Figure 3.7. Representation of the points of interest and their error bars which depict the standard deviation in both coordinates (RD, LT). These points are described in Table 3.4 for case k61. Each colour indicates the maximum and minimum values of each one of the points. Jupiter is at the centre and the Sun is positioned downwards. The dashed lines indicate probable magnetopause locations for compressed (60 R$_J$) and expanded (90 R$_J$) magnetosphere cases.

3.3 Interpretation of the results

In Figure 3.8, one of the simulation results obtained by the MHD model of Fukazawa et al. [2006] is shown. In this figure, the Sun is positioned on the left side. This case has been selected due to the resulting dayside magnetopause location (90 R_J), the same as the one used in the present study. The Interplanetary Magnetic Field (IMF) used for this simulation was equal to 0.105 nT and the solar wind dynamic pressure equal to 0.023 nPa. What is noteworthy here is the region inside the black circle. In Fukazawa et al. [2006] they indicate that this vortex appears because some of the flux coming from the neutral line, which is the reconnection point shown in Figure 1.4, is moving from the duskside to the noonside in a contrary direction to the corotation direction (counterclockwise), therefore producing vortices. Thanks to this vortex, the flow can go back to the reconnection region faster than flowing around Jupiter [Fukazawa et al., 2006].

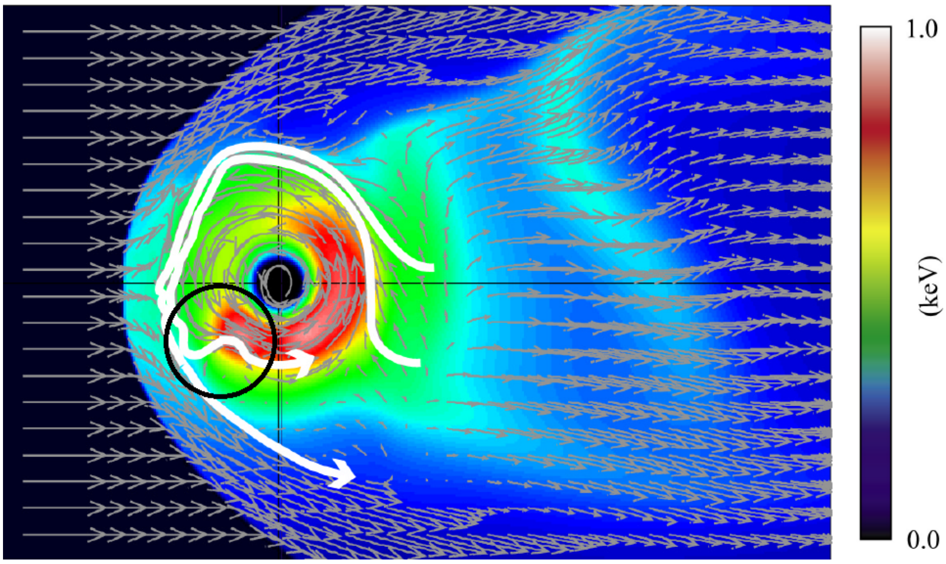

Figure 3.8. Representation of the temperature per atomic mass unit (AMU) values in KeV and plasma flow vectors in the equatorial plane. This figure contains one of the results of the simulation carried out by Fukazawa et al. [2006]. The dynamic pressure is P_d = 0.023 nPa and the IMF is equal to 0.105 nT, producing a dayside magnetopause location of 90 R_J. The black circle indicates the vortex region.

As shown in Figure 3.8, this vortex is found in the same region as the points mapped in the magnetosphere in this study, in the noon-dusk region between approximately 40 R_J and 80 R_J radial distance. Delamere et al. [2013] carried out some simulations of the magnetopause of Saturn in order to show the Kelvin-Helmholtz instability and the resulting vortices. They obtained that the vortices can produce important field-aligned currents and thus electron precipitation in the ionosphere which trigger auroral emissions in the noon and dusk sectors. Grodent et al. [2011] observed some UV auroral features in Saturn such as spots and narrow arcs. They suggested that these emissions could be originated by the vortices caused by the Kelvin-Helmholtz waves. Since it is the vorticity of the plasma flow which is important, the field-aligned currents generated by the Kelvin-Helmholtz vortices can be considered similar to the ones generated by the vortices proposed by Fukazawa et al.

[2006]. **Hence, a possible explanation to Jupiter's auroral bridge could be that these auroral emissions are magnetically connected to the vortices, mapping in the noon-dusk sector, described by Fukazawa et al. [2006].** This agreement between the Fukazawa et al. [2006] model and the magnetospheric region where the auroral bridge is originated is an important result of the present study. Nevertheless, this is a preliminary research of this structure, quite unknown until now. More studies are required in order to give an accurate explanation.

3.4 Emitted power

Tables in Appendix A contain the data of the emitted power by the auroral bridge for each CML as well as the total power emitted by the whole aurora. The maximum, minimum, and mean values of this data are shown in Tables 3.5, 3.6, and 3.7. The power radiated by the auroral bridge was obtained thanks to the RDPIX procedure, as explained in Section 2.4. In some cases, it was difficult to discriminate the emissions from polar flares and the bridge. It is important to be careful in selecting the right area in order not to take into account the incorrect emission.

Value	CML	Power (GW)	Total Power (GW)	Relative power (%)
Mean	175.2	211.4	1654.9	13.1
Max	187.7	442.0	2190	23.5
Min	162.8	63.8	1307	6.2

Table 3.5. Case k24. Maximum, minimum, and mean values of the CML, the power emitted by the auroral bridge, and the total power emitted by the aurora, as well as the percentage of the power emitted by the auroral bridge regarding the total power.

Value	CML	Power (GW)	Total Power (GW)	Relative power (%)
Mean	158.8	425.7	1681.9	26.1
Max	171.3	2089.7	2773.0	75.4
Min	146.3	36.1	1330.0	10.0

Table 3.6. Case k57. Maximum, minimum, and mean values of the CML, the power emitted by the auroral bridge, and the total power emitted by the aurora, as well as the percentage of the power emitted by the auroral bridge regarding the total power.

In case k24, one can observe that the power emitted by the auroral bridge varies between 6.2% and 23.5% of the total power. In case k57, the emitted power is more intense regarding the total emitted power, as shown in Figure 3.12 for example. This leads to a maximum and a minimum value of the relative power of 75.4% and 10% respectively. Finally, in case k61, the relative emitted power varies between 1.9% and 37.6%. The maximum is again higher than in the first case. This big difference between the maximum and the minimum values is caused by the fact that this structure is pulsating and its intensity is consequently unstable (see Section 3.5). Mean values have therefore been obtained. For case k24, it is 13% of the total emitted power. For case k57, it is 26% and for case k61, it is about 10%. The values of k24 and k61 are similar, however in case k57, the mean relative emitted power is larger (a factor of about 2). The case k57 can thus be considered as an extreme case.

Value	**CML**	**Power (GW)**	**Total Power (GW)**	**Relative power (%)**
Mean	176.1	161.5	1365.8	9.8
Max	188.6	815.3	1838.0	37.6
Min	163.7	16.8	1135.0	1.9

Table 3.7. Case k61. Maximum, minimum, and mean values of the CML, the power emitted by the auroral bridge, and the total power emitted by the aurora, as well as the percentage of the power emitted by the auroral bridge regarding the total power.

3.5 Pulsating structure: periodicity

It has been observed that Jupiter's auroral bridge pulsates. Bonfond et al. [2011] reported the periodicity in the power emitted by the polar flares, as explained in Section 1.4.2. Nevertheless, the polar flares and the auroral bridge, when they appear, do not always pulsate simultaneously.

In order to study the periodicity of the power emitted by the auroral bridge, the Lomb-Scargle analysis was carried out using the routine `Lomb_Periodogram_ipc` present in the Appendix B. In Figures 3.9, 3.10, and 3.11, the time evolution of the emitted power by this region and the Lomb-Scargle periodograms are shown. It is important to remember that the sampling of the data is one image every 10 seconds, as explained in Section 2.1.

Case k24

In this case, the maximum peak in the periodogram corresponds to a period of about 150 seconds, i.e., 2.5 minutes (Figure 3.9). Since the P-value[1] of the maximum peak is $7 \cdot 10^{-7}$, the significance level[2] was stablished as 0.01, which led to a confidence level[3] of 99%. However, there are other peaks that stand out among the rest. These peaks correspond to periodicities of 1.1 min, 3.4 min, 5.3 min, and 10.2 min. The last two, that are more important peaks, could correspond to the envelope which seems to appear on the time evolution graph.

Case k57

Contrary to the other two cases, no periodicity emerges from this event. In the Lomb-Scargle periodogram, the maximum peak corresponds to almost 90 seconds, that is, 1.5 minutes (Figure 3.10). In this case the P-value of the maximum peak obtained was 0.33, which indicates a very low relia-

---

[1] The **P-value** of the maximum peak is the probability that such a peak occurred by chance. In order to have a significant peak, the P-value has to be lower or equal to α.

[2] The **significance level** is the probability of failure in the estimation and is represented as α.

[3] The **confidence level** is the probability of success in the estimation. It is calculated as $1 - \alpha$.

bility in the estimation of the maximum peak. This high P-value forced to choose $\alpha = 0.4$, and thus the confidence level is only 60%. In this case, the results are not very reliable since there are a lot of peaks, but none of them is much higher than the others.

Case k61

The maximum peak in the periodogram corresponds to a period of about 83 seconds, i.e., 1.4 minutes (Figure 3.11). There are other three peaks that look important. The periodicities of these peaks are 0.7 min, 1.46 min, 13.7 min. This last peak probably corresponds to the envelope. In this case, the P-value of the maximum peak was $1.4 \cdot 10^{-7}$, even lower than in case k24, which shows a very high reliability. The significance level chosen was therefore 0.01, leading to a confidence level of 99%.

One can observe that in cases k24 and k61 there is one clear peak that indicates the periodicity of the occurrence of the auroral bridge with a high reliability (confidence level of 99%). Nevertheless, even if in case k57 the maximum peak corresponds to 1.5 minutes, the results are less trustworthy (confidence level of 60%). In summary, **the periodicity of this structure varies between 1.5 and 2.5 minutes**. The periodicity of the envelope seems to vary between 10 and 14 minutes.

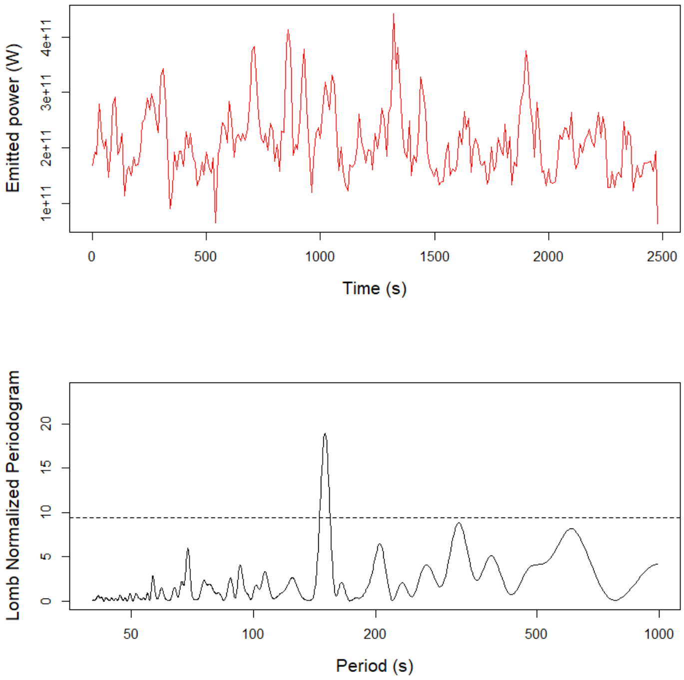

Figure 3.9. Rootname: od8k24ioq. Top: The time evolution of the power emitted by the auroral bridge. Bottom: The Lomb-Scargle periodogram. The dashed line indicates the significance level ($\alpha = 0.01$; confidence level 99%).

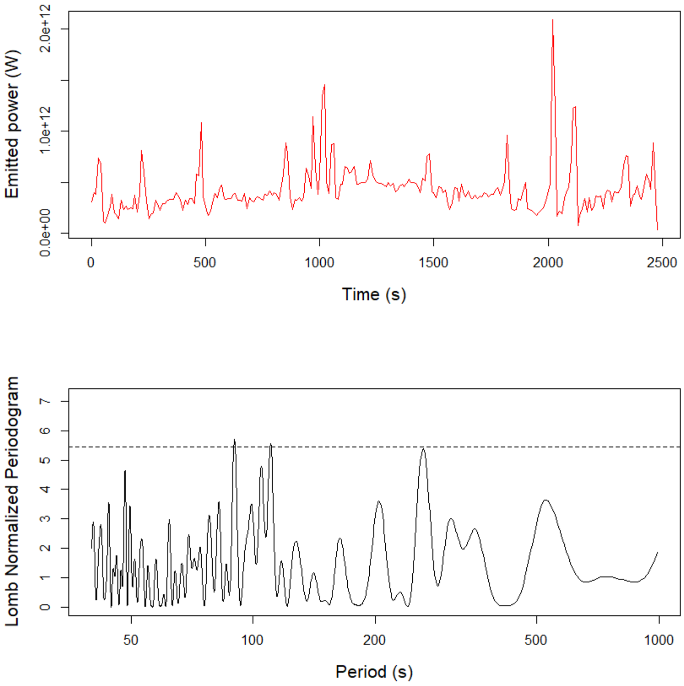

Figure 3.10. Rootname: od8k57itq. Top: The time evolution of the power emitted by the auroral bridge. Bottom: The Lomb-Scargle periodogram. The dashed line indicates the significance level ($\alpha = 0.4$; confidence level 60%).

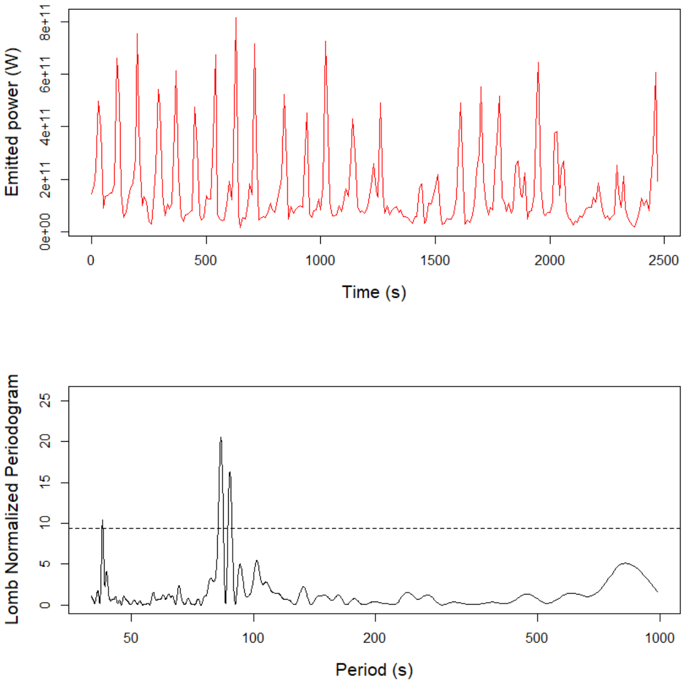

Figure 3.11. Rootname: od8k61lyq. Top: The time evolution of the power emitted by the auroral bridge. Bottom: The Lomb-Scargle periodogram. The dashed line indicates the significance level ($\alpha = 0.01$; confidence level 99%).

In the study of Bonfond et al. [2011] a periodicity of the power emitted by the polar flares between 2 and 3 minutes was found. They suggested that these quasi-periodic flares could originate from the pulsed reconnections and flux transfer events at the dayside magnetopause of Jupiter, similar to the events observed at Earth. In the case of the auroral bridge, the reason for its pulsating behaviour and for the envelope that apparently appears remains unknown. Nevertheless, if the assuption of the vortices created by the flux coming from the reconnection point in the outer magnetosphere is confirmed, the periodicity in the power emitted by the auroral bridge could be associated with the characteristic period of reconnection in the Jovian magnetotail, by analogy with the Bonfond et al. [2011] study. In order to provide an accurate explanation, more specific studies should be conducted.

3.6 Equatorward structure

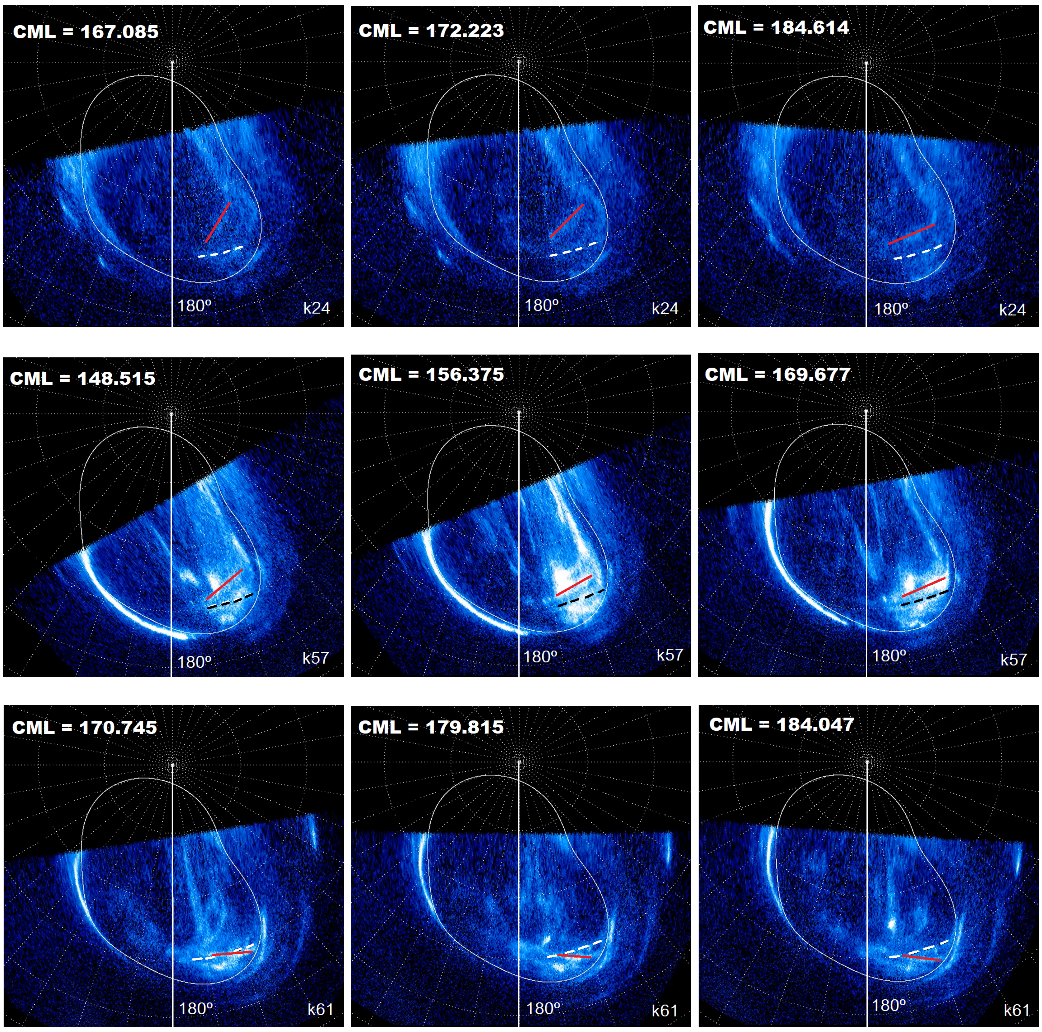

Figure 3.12. Three different frames for each case studied. Top: case k24, centre: case k57, bottom: case k61. A 10° spaced grid is overplotted and the 180° S3 longitude is marked up with the white vertical line. Part of Jupiter's auroral bridge is marked in red and the dashed lines indicate the position of the 60° parallel between S3 longitudes 155° and 175° approximately, in order to have a reference line and to highlight the equatorward movement of this structure.

As explained in the introduction, Grodent et al. [2003b] identified two kinds of structures in the active region: the polar flares and the arc-like feature. The last one was observed to move equatorward when the CML increased. In the present study, this movement was also noticed. Figure 3.12 shows three different frames for each case studied. The CML increases from the image on the left to the image on the right side. Part of the auroral bridge is marked in red. One can observe that this structure is moving equatorward regarding the reference trace (dashed line) indicating the location of the 60^o parallel between S3 longitudes 155^o and 175^o approximately. Therefore, the auroral bridge is sub-corotating with the planet. If this structure is confirmed to be related to the plasma vortices described by Fukazawa et al. [2006], it is expected that the auroral emission should not rotate with the planet, being fixed in MLT (Magnetic Local Time). The equatorward movement could be related to local changes in the magnetosphere. Nevertheless, it will be necessary to study the Jovian magnetosphere in more detail in order to understand its behaviour and its consequences in the auroral emissions.

Chapter 4

Conclusions

Jupiter's aurorae are the most intense in the solar system and they have been studied for almost three decades [Dols et al., 1992]. Nevertheless, there are some auroral features whose origin is still not well understood. One of these structures had been identified as the arc-like feature of the polar active region [Grodent et al., 2003b] or the noon active region [Nichols et al., 2017] in previous studies. Nevertheless, in this document, it has been named Jupiter's auroral bridge as it seems to connect the duskside main emission and the polar region of the northern hemisphere.

To characterise this structure, ultraviolet images collected by the STIS instrument on-board the HST were used. After the observation of several events, three of them (referred to as k24, k57, and k61 in this work) were analysed. In these three cases, the auroral bridge shows subtle differences. In case k24, this structure appears fainter than in the other two events. In k57 and k61, the auroral bridge is quite bright and the intensity is very variable. These two events took place with only three days of difference. Nevertheless, in case k61, this structure appears shifted towards the noon sector in comparison with the other two ones. In most of the cases, two bridges could be identified in each frame, although in case k61, a third one appeared.

In order to obtain the power emitted by this structure and their location in the ionosphere the pixels where this emission appears were selected. Thanks to this data, the region in the magnetosphere where the auroral bridge is originating could be revealed using mapping models. Two methods were carried out. The first method consisted in tracing field lines from three global field models (GAM, JRM09, and Khurana). The second one, obtained the points in the equatorial plane by the flux equivalence calculation described by Vogt et al. [2011]. This last model needs to use other internal field models. To this aim, GAM and JRM09 were used. Since each model has different restrictions, the mean and the standard deviation of the positions obtained by the five calculations were determined, in order to better estimate the location of the mapped points. In the three cases, the points were mapped in the noon-dusk region, between 11:00 LT and 20:00 LT, and between 40 R_J and 100 R_J radial distances. Nevertheless, the points of case k61 shifted towards the noon sector, which corresponds to the different position of this structure in the ionosphere.

The simulation results of the MHD model of Fukazawa et al. [2006] showed that in the noon-dusk region, vortices are created because there is some flux coming from the neutral line, in a contrary direction to the one of the corotation. As suggested by Delamere et al. [2013] and Grodent et al. [2011], these vortices can produce important field-aligned currents and, consequently, the electron precipitation in the ionosphere which produces auroral emissions. Therefore, the plasma vortices in the magnetosphere could be magnetically connected to the auroral bridge.

The relative power emitted by this structure was calculated. The mean values indicated that for events k24 and k61 the radiated power is about 10-13% of the total emitted power, while for k57 it is 26%. The last case can thus be considered as an extreme case.

Since the auroral bridge pulsated, its periodicity of occurrence was studied. Thanks to a Lomb-Scargle analysis, the period obtained was between 1.5 and 2.5 minutes. Moreover, another peak on the periodograms was noticeable. This peak matched a periodicity of 10-14 minutes and could correspond to the apparent envelope shown on the time evolution graphs. If the assuption of the plasma vortices described by Fukazawa et al. [2006] is the origin of the auroral bridge and by analogy with the Bonfond et al. [2011] study, this periodicity in the emitted power could be related to the characteristic period of reconnection in the outer magnetosphere of Jupiter.

In this study, it was observed that the auroral bridge moves equatorward when the CML increases. Previously, this behaviour had also been reported by Grodent et al. [2003b].

An important constraint of this study is that the locations in the ionosphere are selected by hand and therefore there could be some human error. Nevertheless, since about 250 images were analysed for each case, this error has been minimised.

It is important to remember that this study is a first analysis of Jupiter's auroral bridge, which has not been analysed in depth previously. In this report, some preliminary results have been produced in order to help future studies. Besides, an analysis of this structure in the southern hemisphere could shed more light on this phenomenon. The Juno mission will be the key to understanding the processes of the Jovian magnetosphere.

References

Badman, S. V., Branduardi-Raymont, G., Galand, M., Hess, S. L. G., Krupp, N., Lamy, L., Melin, H., and Tao, C. (2014). Auroral processes at the giant planets: Energy deposition, emission mechanisms, morphology and spectra. *Space Science Reviews*, 187:99–179.

Bagenal, F. (2013). Planetary magnetospheres. In *Solar and Stellar Planetary Systems*, pages 251–307. Springer, Dordrecht.

Bagenal, F., Adriani, A., Allegrini, F., Bolton, S. J., Bonfond, B., Bunce, E. J., Connerney, J. E. P., Cowley, S. W. H., Ebert, R. W., Gladstone, G. R., Hansen, C. J., Kurth, W. S., Levin, S. M., Mauk, B. H., McComas, D. J., Paranicas, C. P., Santos-Costa, D., Thorne, R. M., Valek, P., Waite, J. H., and Zarka, P. (2014). Magnetospheric science objectives of the Juno mission. *Space Science Reviews*.

Bagenal, F., Dowling, T. E., and McKinnon, W. B. (2004). Introduction. In *Jupiter: the planet, satellites and magnetosphere*, chapter 1, pages 1–18. Cambridge University Press.

Bagenal, F. and Wilson, R. J. (2016). Jupiter coordinate systems.

Bolton, S., Levin, S., and Bagenal, F. (2017a). Juno's first glimpse of Jupiter's complexity. *Geophysical Research Letters*, 44:7663–7667.

Bolton, S. J., Adriani, A., Adumitroaie, V., Allison, M., Anderson, J., Atreya, S., Bloxham, J., Brown, S., Connerney, J. E. P., DeJong, E., Folkner, W., Gautier, D., Grassi, D., Gulkis, S., Guillot, T., Hansen, C., Hubbard, W. B., Iess, L., Ingersoll, A., Janssen, M., Jorgensen, J., Kaspi, Y., Levin, S. M., Li, C., Lunine, J., Miguel, Y., Mura, A., Orton, G., Owen, T., Ravine, M., Smith, E., Steffes, P., Stone, E., Stevenson, D., Thorne, R., Waite, J., Durante, D., Ebert, R. W., Greathouse, T. K., Hue, V., Parisi, M., Szalay, J. R., and Wilson, R. (2017b). Jupiter's interior and deep atmosphere: The initial pole-to-pole passes with the Juno spacecraft. *Science*, 356(6340):821–825.

Bonfond, B., Grodent, D., Badman, S. V., Saur, J., Gérard, J.-C., and Radioti, A. (2017). Similarity of the Jovian satellite footprints: Spots multiplicity and dynamics. *Icarus*, 292:208–217.

Bonfond, B., Grodent, D., Gérard, J.-C., Radioti, A., Dols, V., Delamere, P. A., and Clarke, J. T. (2009). The Io UV footprint: Location, inter-spot distances and tail vertical extent. *Journal of Geophysical Research: Space Physics*, 114(A07224).

Bonfond, B., Vogt, M. F., Gérard, J.-C., Grodent, D., Radioti, A., and Coumans, V. (2011). Quasi-periodic polar flares at Jupiter: A signature of pulsed dayside reconnections? *Geophysical Research Letters*, 38(L02104).

Clarke, J. T., Grodent, D., Cowley, S. W. H., Bunce, E. J., Zarka, P., Connerney, J. E. P., and Satoh, T. (2004). Jupiter's aurora. In *Jupiter: the planet, satellites and magnetosphere*, chapter 26, pages 639–670. Cambridge University Press.

Connerney, J. E. P., Acuña, M. H., Ness, N. F., and Satoh, T. (1998). New models of Jupiter's magnetic field constrained by the Io flux tube footprint. *Journal of Geophysical Research: Space Physics*, 103(A6):11929–11939.

Connerney, J. E. P., Kotsiaros, S., Oliversen, R. J., Espley, J. R., Jørgensen, J. L., Joergensen, P. S., Merayo, J. M. G., Herceg, M., Bloxham, J., Moore, K. M., Bolton, S. J., and M, L. S. (2018). A new model of Jupiter's magnetic field from Juno's first nine orbits. *Geophysical Research Letters*, 45:2590–2596.

Cowley, S. W. H., Bunce, E. J., Stallard, T. S., and Miller, S. (2003). Jupiter's polar ionospheric flows: Theoretical interpretation. *Geophysical research letters*, 30(5).

Cravens, T. E. (1997). Magnetohydrodynamics. In *Physics of solar system plasmas*, chapter 4, pages 90–158. Cambridge University Press.

Delamere, P. A., Wilson, R. J., Eriksson, S., and Bagenal, F. (2013). Magnetic signatures of Kelvin-Helmholtz vortices on Saturn's magnetopause: Global survey. *Journal of Geophysical Research: Space Physics*, 118:393–404.

Dols, V., Gérard, J.-C., Paresce, F., Prangé, R., and Vidal-Madjar, A. (1992). Ultraviolet imaging of the Jovian aurora with the Hubble Space Telescope. *Geophysical research letters*, 19(18):1803–1806.

Fukazawa, K., Ogino, T., and Walker, R. J. (2006). Configuration and dynamics of the jovian magnetosphere. *Journal of Geophysical Research: Space Physics*, 111(A10207).

Grodent, D. (2014). A brief review of ultraviolet auroral emissions on giant planets. *Space Science Reviews*, 187(1-4):23–50.

Grodent, D. (2019). Lecture notes in Planetary Magnetospheres and Aurorae. Université de Liège.

Grodent, D., Bonfond, B., Gérard, J.-C., Radioti, A., Gustin, J., Clarke, J. T., Nichols, J., and Connerney, J. E. P. (2008a). Auroral evidence of a localized magnetic anomaly in Jupiter's northern hemisphere. *Journal of Geophysical Research: Space Physics*, 113(A09201).

Grodent, D., Bonfond, B., Yao, Z. H., Gérard, J.-C., Radioti, A., Dumont, M., Palmaerts, B., Adriani, A., Badman, S. V., Bunce, E., et al. (2018). Jupiter's aurora observed with HST during Juno orbits 3 to 7. *Journal of Geophysical Research: Space Physics*, 123.

Grodent, D., Clarke, J. T., Kim, J., Waite Jr., J. H., and Cowley, S. W. H. (2003a). Jupiter's main auroral oval observed with HST-STIS. *Journal of Geophysical Research: Space Physics*, 108(A11).

Grodent, D., Clarke, J. T., Waite Jr., J. H., Cowley, S. W. H., Gérard, J.-C., and Kim, J. (2003b). Jupiter's polar auroral emissions. *Journal of Geophysical Research: Space Physics*, 108(A10).

Grodent, D., Gérard, J.-C., Radioti, A., Bonfond, B., and Saglam, A. (2008b). Jupiter's changing auroral location. *Journal of Geophysical Research: Space Physics*, 113(A01206).

Grodent, D., Gustin, J., Gérard, J.-C., Radioti, A., Bonfond, B., and Pryor, W. R. (2011). Small-scale structures in Saturn's ultraviolet aurora. *Journal of Geophysical Research: Space Physics*, 116(A09225).

Guillot, T., Stevenson, D. J., Hubbard, W. B., and Saumon, D. (2004). The interior of Jupiter. In *Jupiter: the planet, satellites and magnetosphere*, chapter 3, pages 35–57. Cambridge University Press.

Gustin, J., Bonfond, B., Grodent, D., and Gérard, J.-C. (2012). Conversion from HST ACS and STIS auroral counts into brightness, precipitated power, and radiated power for H_2 giant planets. *Journal of Geophysical Research: Space Physics*, 117(A07316).

Hess, S. L. G., Bonfond, B., Zarka, P., and Grodent, D. (2011). Model of the Jovian magnetic field topology constrained by the Io auroral emissions. *Journal of Geophysical Research: Space Physics*, 116(A5).

Joy, S. P., Kivelson, M. G., Walker, R. J., Khurana, K. K., Russell, C. T., and Ogino, T. (2002). Probabilistic models of the Jovian magnetopause and bow shock locations. *Journal of Geophysical Research: Space Physics*, 107(A10).

Khurana, K. Magnetospheres of the Outer Planets Group. Laboratory for Atmospheric and Space Physics. Retrieved from `http://lasp.colorado.edu/home/mop/resources/graphics/code/?doing_wp_cron=1564072762.0219609737396240234375`.

Khurana, K. K., Kivelson, M. G., Vasyliunas, V. M., Krupp, N., Woch, J., Lagg, A., Mauk, B. H., and Kurth, W. S. (2004). The configuration of Jupiter's magnetosphere. In *Jupiter: the planet, satellites and magnetosphere*, chapter 24, pages 593–616. Cambridge University Press.

NASA. (NASA, a). Hubblesite. Mission and Telescope. Retrieved from `https://hubblesite.org/mission-and-telescope`.

NASA. (NASA, b). New Horizons. Retrieved from `https://www.nasa.gov/mission_pages/newhorizons/main/index.html`.

NASA. (NASA, c). Solar System Exploration. Galileo. Retrieved from `https://solarsystem.nasa.gov/missions/galileo/overview/`.

NASA. (NASA, d). Solar System Exploration. Jupiter. Retrieved from `https://solarsystem.nasa.gov/planets/jupiter/overview/`.

NASA. (NASA, e). Space Telescope Science Institute. Space Telescope Imaging Spectrograph. Retrieved from `http://www.stsci.edu/hst/stis`.

Nichols, J. D., Badman, S. V., Bagenal, F., Bolton, S. J., Bonfond, B., Bunce, E. J., Clarke, J. T., Connerney, J. E. P., Cowley, S. W. H., Ebert, R. W., Fujimoto, M., Gérard, J.-C., Gladstone, G. R., Grodent, D., Kimura, T., Kurth, W. S., Mauk, B. H., Murakami, G., McComas, D. J., Orton, G. S., Radioti, A., Stallard, T. S., Tao, C., Valek, P. W., Wilson, R. J., Yamazaki, A., and Yoshikawa, I. (2017). Response of Jupiter's auroras to conditions in the interplanetary medium as measured by the Hubble Space Telescope and Juno. *Geophysical Research Letters*, 44:7643–7652.

Palmaerts, B. (2013). Morphologie de l'émission aurorale UV principale de Jupiter en fonction du temps local. Master's thesis, Université de Liège, Belgium.

Radioti, A., Gérard, J.-C., Grodent, D., Bonfond, B., Krupp, N., and Woch, J. (2008). Discontinuity in Jupiter's main auroral oval. *Journal of Geophysical Research*, 113(A01215).

Taylor, F. W., Atreya, S. K., Encrenaz, T., Hunten, D. M., Irwin, P. G. J., and Owen, T. C. (2004). The composition of the atmosphere of Jupiter. In *Jupiter: the planet, satellites and magnetosphere*, chapter 4, pages 59–78. Cambridge University Press.

Vasyliunas, V. M. (1983). Plasma distribution and flow. In *Physics of the Jovian magnetosphere*, pages 395–453. Cambridge University Press.

Vogt, M. F., Bunce, E. J., Kivelson, M. G., Khurana, K. K., Walker, R. J., Radioti, A., Bonfond, B., and Grodent, D. (2015). Magnetosphere-ionosphere mapping at Jupiter: Quantifying the effects of using different internal field models. *Journal of Geophysical Research: Space Physics*, 120:2584–2599.

Vogt, M. F., Kivelson, M. G., Khurana, K. K., Walker, R. J., Bonfond, B., Grodent, D., and Radioti, A. (2011). Improved mapping of Jupiter's auroral features to magnetospheric sources. *Journal of Geophysical Research: Space Physics*, 116(A03220).

Waite Jr., J. H., Gladstone, G. R., Lewis, W. S., Goldstein, R., McComas, D. J., Riley, P., Walker, R. J., Robertson, P., Desai, S., Clarke, J. T., and Young, D. T. (2001). An auroral flare at Jupiter. *Nature*, 410:787–789.

Yao, Z. H., Grodent, D., Kurth, W. S., Clark, G., Mauk, B. H., Kimura, T., Bonfond, B., Ye, S.-Y., Lui, A. T., Radioti, A., Palmaerts, B., Dunn, W. R., Ray, L. C., Bagenal, F., Badman, S. V., Rae, I. J., Guo, R. L., Pu, Z. Y., Gérard, J.-C., Yoshioka, K., Nichols, J. D., Connerney, J. E. P., Bolton, S., and Levin, S. M. On the relation between Jovian aurorae and the loading/unloading of the magnetic flux: simultaneous measurements from Juno, HST and Hisaki. Unpublished.